Status Report on Laboratory Testing and International Collaborations in Salt

Spent Fuel and Waste Disposition

Prepared for
US Department of Energy
Spent Fuel and Waste Science and Technology

Kristopher L. Kuhlman, Edward N. Matteo,
Teklu Hadgu, Benjamin Reedlunn,
Steven R. Sobolik, Melissa M. Mills,
Leslie D. Kirkes, Yongliang Xiong,
Jonathan P. Icenhower
Sandia National Laboratories

September 30, 2017
SFWD-SFWST-2017-000100

DISCLAIMER

This information was prepared as an account of work sponsored by an agency of the U.S. Government. Neither the U.S. Government nor any agency thereof, nor any of their employees, makes any warranty, expressed or implied, or assumes any legal liability or responsibility for the accuracy, completeness, or usefulness, of any information, apparatus, product, or process disclosed, or represents that its use would not infringe privately owned rights. References herein to any specific commercial product, process, or service by trade name, trade mark, manufacturer, or otherwise, does not necessarily constitute or imply its endorsement, recommendation, or favoring by the U.S. Government or any agency thereof. The views and opinions of authors expressed herein do not necessarily state or reflect those of the U.S. Government or any agency thereof.

Sandia National Laboratories is a multimission laboratory managed and operated by National Technology and Engineering Solutions of Sandia LLC, a wholly owned subsidiary of Honeywell International Inc. for the U.S. Department of Energy's National Nuclear Security Administration under contract DE-NA0003525.

SUMMARY

This report is a summary of the international collaboration and laboratory work funded by the US Department of Energy Office of Nuclear Energy Spent Fuel and Waste Science & Technology (SFWST) as part of the Sandia National Laboratories Salt R&D work package. This report satisfies milestone level-four milestone M4SF-17SN010303014. Several stand-alone sections make up this summary report, each completed by the participants. The first two sections discuss international collaborations on geomechanical benchmarking exercises (WEIMOS) and bedded salt investigations (KOSINA), while the last three sections discuss laboratory work conducted on brucite solubility in brine, dissolution of borosilicate glass into brine, and partitioning of fission products into salt phases.

This page is intentionally left blank.

CONTENTS

SUMMARY iii

ACRONYMS x

1. International Collaboration through the KOSINA Project 2
   1.1 Reference 3

2. International Collaboration through the Joint Project WEIMOS 4
   2.1 Reconstruction of Room D Closure Data 4
   2.2 Shear Behavior of Stratigraphic Interfaces 4
   2.3 Creep Mechanism at Low Deviatoric Stresses 4
   2.4 Update to the Munson Dawson Model 5
   2.5 References 5

3. Experimental Determination of Brucite Solubility in NaCl Solutions at Elevated Temperatures 7
   3.1 Introduction 7
   3.2 Methods 7
   3.3 Experimental Results and Thermodynamic Calculations 8
      3.3.1 Correction Factors at Elevated Temperatures as a Function of Ionic Strength 8
      3.3.2 Solubility of Brucite in NaCl Solutions at Elevated Temperatures 9
   3.4 Conclusions 12
   3.5 References 12

4. Dissolution of Borosilicate Glass into Brine Solutions 14
   4.1 Introduction 14
   4.2 Experimental Process Description 15
      4.2.1 Overall Strategy and Process 15
         4.2.1.1 Single-Pass Flow-Through (SPFT) Experiments 15
         4.2.1.2 Static Experiments 18
   4.3 Materials 18
   4.4 Results 19
      4.4.1 Single-Pass Flow-Through (SPFT) 19
         4.4.1.1 NaCl Solutions 19
         4.4.1.2 $MgCl_2$ & Mixed (NaCl-$MgCl_2$) Solutions 22
      4.4.2 Static Experiments 24
   4.5 Conclusions 24
   4.6 References 24

5. Partitioning of Fission Products (Cs, Sr, and I) into Salt Phases 26
   5.1 Introduction 26

5.2 Experimental Process Description 26
5.2.1 Overall Strategy and Process 26
5.2.2 Experimental Procedure 27
5.2.3 Electron Microprobe Analysis (EMPA) 28
5.2.4 Solution Analyses (ICP-AES, -MS and IC) 29
5.2.5 X-ray Diffraction (XRD) 29
5.2.6 Scanning Electron Microscopy (SEM) 29
5.3 Results 29
5.3.1 Sylvite [KCl] 29
5.3.2 Gypsum [CaSO4·2H2O] 30
5.3.3 Langeinite [$K_2Mg_2(SO_4)_3$] (or the K_2SO_4-$MgSO_4$-H_2O System) 32
5.3.4 Carnallite [$KMgCl_3 \cdot 6H_2O$] 35
5.4 Conclusions and Recommendations for Future Studies 36
5.5 References 37

This page is intentionally left blank.

LIST OF FIGURES

Figure 1. Schematic of the Single-Pass Flow-Through (SPFT) system 17

Figure 2. Left (A): Cartoon of interferometric technique for determining glass monolith dissolution rates. Right (B): A three-dimensional height map of a portion of the reference and reacted surfaces of a glass monolith exposed to solution at 90°C 18

Figure 3. Approach to steady-state conditions for monoliths (A left) and powders (B right). The figures show the release of Si from glass to solution 19

Figure 4. (A left) Dissolution rate (based on measured Si release to effluent) versus NaCl for both monoliths and powders. (B right) Dissolution rate versus NaCl up to 0.6 m illustrating the effect of NaCl on borosilicate glass. 20

Figure 5. Normalized Rates (rates in NaCl solutions/average rates in NaCl-free solutions) versus NaCl for (A top left) β-quartz, (B bottom left) $aSiO_2$ (amorphous silica), (C top right) ISG borosilicate glass (this work), and (D bottom right) all three solids on the same plot. 21

Figure 6. Dissolution rate (based on Si release) versus NaCl concentration. Rates for monoliths and powders are distinguished. The data suggest that the dissolution rate in concentrated brines is governed by the decrease in the activity of water....22

Figure 7. Dissolution rate versus $MgCl_2$ concentration. Rates were determined by Si assay in $MgCl_2$ (red circles), in simplified synthetic brine (GWB; green squares) and by interferometry (blue triangles). Powders and monoliths are not differentiated on this figure. Note that the dissolution rate of ISG in the synthetic GWB is indistinguishable from the rates in $MgCl_2$ only. 23

Figure 8. Normalized dissolution rate versus concentration of either NaCl or $MgCl_2$ 23

Figure 9. SEM image of typical sylvite crystals (light grey) exhibiting “skeletal” appearance. The scale bar (100 μm) is located on the center bottom of the image. 30

Figure 10. Typical SEM images of precipitated gypsum. With high Sr concentrations (600 ppm initial), as seen in Image C, the gypsum crystals are relatively small and are accompanied by celestite ($SrSO_4$). 31

Figure 11. SEM image of gypsum (A) and corresponding x-ray maps illustrating the distribution of Ca, Sr, and S (B, C and D, respectively) in the crystals. 32

Figure 12. Backscattered electron image of precipitates from an experiment at 90 ºC. Light grey represents langbeinite, medium grey leonite, dark grey $MgSO_4$ and black epoxy. Note the porous rim around the edge of the leonite indicating it is unstable. 33

Figure 13. Backscattered electron image of a langbeinite crystal (light grey) surrounded by porous leonite (medium grey), $MgSO_4$ (dark grey) and epoxy (black). 34

Figure 14. X-ray maps of langbeinite (same as depicted in Fig. 5). K Kα (A), Mg Kα (B), Cs Lα (C) and S Kα (D). The x-ray maps indicate that Cs is relatively homogeneously distributed in the langbeinite and that more Cs is present in langbeinite compared to leonite. 35

Figure 15. SEM image of a large carnallite crystal. The scale bar (100 μm) is located on the center bottom of the image. 36

LIST OF TABLES

Table 1. Experimentally determined pH correction factors at different temperatures as a function of ionic strength 9

Table 2. Concentration dependence of pH correction factors at constant temperatures 9

Table 3. Equilibrium quotients for Reaction (3.3) determined in this study 11

Table 4. Equilibrium constants for Reaction (3.3) at infinite dilution determined in this work 12

Table 5. Chemical composition of ISG glass in mole % and weight % oxides. 19

ACRONYMS

AES	atomic emission spectrometer
BGR	Bundesanstalt für Geowissenschaften und Rohstoffe (German Geological Survey)
BSE	backscattered electrons
CCD	charge-coupled device
DI	deionized
DOE	Department of Energy
DWR	Defense Waste Repository
EDS	energy dispersive spectroscopy
EMPA	electron microprobe analysis
FP	fission product
IC	ion chromatography
ICP	inductively coupled plasma
IfG	Institut für Gebirgsmechanik GmbH (Institute for Geomechanics)
GWB	G-seep WIPP brine
ISG	International Simple Glass
KOSINA	Konzeptentwicklung für ein generisches Endlager für wärmeentwickelnde Abfälle in flach lagernden Salzschichten in Deutschland sowie Entwicklung und Überprüfung eines Sicherheits- und Nachweiskonzeptes (Concept development for a generic repository for heat generating waste in bedded salt formation as well as development and review of a safey and verification project).
LLQ	lower limit of quantification
MD	Munson-Dawson (constitutive model)
MS	mass spectrometry
R&D	Research and Development
SEM	scanning electron microscopy
SIT	specific ion interaction theory
SFWST	Spent Fuel and Waste Science & Technology
SNL	Sandia National Laboratories
SPFT	Single-Pass Flow-Through
US	United States
WEIMOS	Weiterentwicklung und Qualifizierung der gebirgsmechanischen Modellierung für die HAW-Endlagerung im Steinsalz (Further Development and Qualification of the Rock Mechanical Modeling for the Final HLW Disposal in Rock Salt)
WIPP	Waste Isolation Pilot Plant
XRD	X-ray diffraction

This page is intentionally left blank.

STATUS REPORT ON LABORATORY TESTING AND INTERNATIONAL COLLABORATIONS IN SALT

This report is a summary of the international collaboration and laboratory work funded by the US Department of Energy Office of Nuclear Energy Spent Fuel and Waste Science & Technology (SFWST) as part of the Sandia National Laboratories Salt R&D work package. Five stand-alone sections make up this summary report, each section completed by different participants. The first two sections discuss international collaborations on geomechanical benchmarking exercises (WEIMOS) and bedded salt investigations (KOSINA), while the last three sections discuss laboratory work conducted on brucite solubility in brine, dissolution of borosilicate glass into brine, and partitioning of fission products into salt phases.

Two of the primary collaborative efforts funded by Salt R&D are co-organization of, and participation in, both the US/German Workshop on Salt Repository Research, Design, and Operation and the NEA Salt Club. The seventh meeting of the Salt Club took place September 4, 2017. The eighth meeting of the US/German workshop took place in The Netherlands September 5-7, 2017, both at the COVRA facilities near Middelburg. These international collaborations will be summarized in detail in the upcoming proceedings, which will be a milestone completed in fiscal year 2018.

Because each of the major sections of this report stands alone, each has its own conclusions and there is no overall summary or conclusions at the end.

1. International Collaboration through the KOSINA Project

Authors: *Ed Matteo* (SNL), *Teklu Hadgu* (SNL), and *Eric Simo* (DBE TEC)

The 7th US/German Workshop on Salt Repository Research, Design and Operation held in Washington D.C. in early September 2016 (Hansen et al. 2017) provided an opportunity for German and US researchers associated with KOSINA (Concept development for a generic final repository for heat-generating wastes in flat-bedded salt layers in Germany as well as development and examination of a safety and verification concept) to exchange information and share preliminary results. Both the US and German programs are conducting research on thermal analysis of emplaced waste packages. Thermomechanical response of the disposal system will govern concepts of operation and be used to determine waste package spacing, drift geometry and underground layout, operational safety, sealing strategy, and ultimately the overall lateral extent of a repository design. In addition to spacing geometry, thermal analyses test other model parameter sensitivity, such as varying surface storage time before disposal, thermal conductivity of host media, engineered barrier system design elements, and thermal output per waste package for different waste types. Given the overlap between KOSINA and ongoing activities in the US-DOE initiatives evaluating repository conditions with lower thermal loading, thermal analysis was identified as an area for research collaboration and exchange.

Following up on 2016 meetings in March at BGR (Bundesanstalt für Geowissenschaften und Rohstoffe) and the 7th US/German Workshop in Sept-member, representatives from the US-DOE visited Hannover, Germany in March 2017 to attend the jointly scheduled meeting of the KOSINA and WEIMOS (Further Development and Qualification of the Rock Mechanical Modeling for the Final HLW Disposal in Rock Salt) Projects (see Section 2 summarizing WEIMOS-related collaborations). During the 2017 Meeting in Germany, and during subsequent monthly video conferences held from March until September, a plan to collaborate on a benchmarking was formalized. The results will be presented at the Waste Management 2018 Conference in Phoenix, AZ. A summary of the benchmarking study is available in Section 2.4 below.

As part of the repository design process, the configuration of the waste packages in the repository can be optimized under the requirement that the maximum temperature in the repository is below the temperature limit of the host rock. Several methods are available to perform this thermal analysis. The methods include simpler semi-analytical codes that provide quick analysis of heat transport, and the more complex numerical methods that provide distributions of heat, often coupled to mechanical phenomena and fluid flow. The aim of the present collaborative study is to compare the capabilities and assess the validity of such codes used in Germany and the United States against field and laboratory observations. To this effect, a US-German working group has been set up between DBE Technology GmbH (DBE) and Sandia National Laboratories.

The code benchmarking studies are based on two disposal concepts. The first one is a German drift disposal layout designed by DBE. Thermal analysis was based on the numerical code FLAC3D and the semi-analytical code LinSour. LinSour is based on the analytical solution of the heat transfer differential equation and has been in use for 25 years by DBE mbH and DBE Technology GmbH. The thermal analysis of this disposal concept was also carried out by Sandia National Laboratories using a semi-analytical code implemented in Mathcad 14. The second concept is a US disposal layout from Sandia National Laboratories. Thermal analysis was carried out at Sandia National Laboratories using the semi-analytical method implemented using Mathcad 14. Thermal analysis of this example was also done by DBE with the codes FLAC3D and LinSour. The thermal simulations at both DBE and Sandia National Laboratories used the same original input parameters. The studies include comparisons of results, which will be used to assess and improve the performance of the codes.

1.1 Reference

Hansen, F.D., W. Steininger & W. Bollingerfehr, 2017. *Proceedings of the 7th US/German Workshop on Salt Repository Research, Design, and Operation*. SFWD-SFWST-2017-000008, Albuquerque, NM: Sandia National Laboratories.

2. International Collaboration through the Joint Project WEIMOS

Authors: *Benjamin Reedlunn* (SNL), *Steve Sobolik* (SNL), and *Melissa Mills* (SNL)

Sandia National Laboratories staff have been collaborating with German salt researchers over the last several years to improve models for the thermo-mechanical behavior of rock salt. The most recent of these collaborations is Joint Project WEIMOS. The participants in the Joint Projects calibrate their salt constitutive models against simple laboratory tests, and benchmark the models against more complex laboratory or underground experiments. This process helps identify deficiencies in both the constitutive model and the methods used to simulate the complex experiments. Further research hopefully reduces existing discrepancies, and eventually leads to improved constitutive models and simulation techniques. The next several sub-sections summarize Sandia's contributions (some of which are being funded by WIPP) to Joint Project WEIMOS during fiscal year 2017.

2.1 Reconstruction of Room D Closure Data

Both Joint Project WEIMOS and its precursor, Joint Project III, have focused on simulating the closure of Room D at the Waste Isolation Pilot Plant (WIPP). As shown in Reedlunn (2016), the Munson-Dawson model under predicted Room D's vertical closure by 3.1 times at 3.7 years. Other Joint Project partners reported fairly similar results (see Hampel (2016)), causing them to question the closure measurements collected in the 1980's. Room D was excavated using a multi-pass mining sequence, which destroyed the closure measurement stations with each pass. The process of zeroing and shifting the raw closure measurements after each mining pass was not well documented in Munson et al. (1988) or Munson et al. (1992). Consequently, the raw closure measurements taken from the WIPP archives, were digitized and reanalyzed. The reconstructed closure data matched the plots in Munson et al. (1989) to within ±5% at 4 years of closure. These results will be documented in an upcoming SAND report.

2.2 Shear Behavior of Stratigraphic Interfaces

The Room D study during Joint Project III also highlighted a gap in the WIPP geomechanical modeling strategy. The interfaces between stratigraphic layers are known to slide relative to one another as rooms close, and the sliding is thought to have first-order effects on roof collapse, room closure, and interface permeability to fluid flow. Despite their importance, characterizations of the peak shear strength, residual shear strength, and permeability of interfaces in salt are extremely rare in the published literature. As such, simulations of WIPP room closure simply use Coulomb friction, with a coefficient of friction of 0.2.

Sandia is beginning to improve the understanding of salt interface mechanics with a laboratory test program at WIPP. This fiscal year, Sandia has partnered with RE/SPEC (Rapid City, SD), to obtain and test salt cores (with interfaces) similar to those found at the WIPP. Core drilling sites have been selected with salt/clay/salt, anhydrite/salt, and polyhalite/salt interfaces. Extraction is planned for September 2017, and direct shear testing on 4-inch diameter specimens should begin shortly thereafter. The results from these tests will be shared with Joint Project WEIMOS partners to help develop constitutive models for the interface behavior. Larger *in-situ* tests are planned to determine how the laboratory tests on these 4 inch specimens translate to the field scale.

2.3 Creep Mechanism at Low Deviatoric Stresses

Joint Project III confirmed that salt undergoes a creep mechanism change between intermediate and low deviatoric stresses. Furthermore, models that incorporate the different creep behavior at low stresses predict significantly greater rates of room closure (see Hampel (2016)). Multiple theories, such as cross-slip, grain boundary sliding, Coble, and Harper-Dorn creep, have been proposed for the new creep mechanism at low stresses, but none have been confirmed. Without a definitive mechanism, rock salt constitutive models must be calibrated against an extensive series of tests at these low stresses. Thus, Sandia and Bundesanstalt für Geowissenschaften und Rohstoffe (BGR) agreed to perform observational

microscopy, attempting to distinguish and identify associated deformation mechanisms. During the March 28th, 2017 visit, German colleagues at Institut für Gebirgsmechanik GmbH (IfG) provided eight samples of creep tested intact WIPP salt cores to Sandia colleagues at the 6th WEIMOS workshop in Hannover, Germany.

The WIPP test plan describes general techniques and equipment for observational microscopy of natural and laboratory tested salt. The experimental process for the low deviatoric stress samples will be similar to details in the test plan. Since salt samples were tested from intact sub-samples, grain boundaries will have higher cohesion and grain plucking may be too difficult without disturbing the sample. Therefore, to minimize any damage effects, original surfaces will be polished and examined under reflected light on the optical microscope before disturbing the sample through mechanical loading or creating thin sections. Additional activities to be performed include the use of a scanning electron microscope for higher resolution, creating thin sections to observe photoelastic features, and etching surfaces and/or thin sections to examine subgrain size and free dislocation density, examine grain boundaries for evidence of other mechanisms, and compare results to literature and BGR conclusions.

2.4 Update to the Munson Dawson Model

Sandia's participation in Joint Project III brought out three shortcomings of the Munson-Dawson (MD) constitutive model for the thermomechanical behavior of salt. Sandia has largely resolved them as part of Joint Project WEIMOS. More specifically:

1. The MD model failed to capture the creep behavior at low deviatoric stresses, so a new steady-state creep term and a new transient creep term were added to the model. These terms will be calibrated against the suite of tests on WIPP salt by Joint Project WEIMOS. If the Sandia and BGR microscopy studies reveal a definitive creep mechanism, the new phenomenological creep terms may be replaced with more scientifically-based representations.
2. The MD model originally used a von Mises equivalent stress, but the equivalent stress measure was changed to Tresca in order to better match true tri-axial creep experiments on hollow cylinders in Munson et al. (1989). The revised match, however, does not reproduce closely the observations at a Lode angle of 20º. This deficiency was remedied by replacing the Tresca flow potential with the Hosford (1972) flow potential, whose parameters can be tuned to represent Tresca, von Mises, or a continuum of shapes in-between.
3. The two numerical formulations of the MD model in Sierra/Solid Mechanics were not robust. The old explicit formulation would virtually halt in the middle of a simulation because it would calculate an exceedingly small critical time step relative to the finite element code time step. The old implicit formulation was an improvement, but it would frequently fail to converge. Thus, a new implicit formulation was implemented in Sierra/Solid Mechanics, and it proved to be roughly 10X faster than the old implicit formulation for a benchmark simulation of Room D closure.

Once the aforementioned changes were implemented, the new MD model implementation was verified against two analytical solutions and by comparing the three model formulations in a room closure simulation. Next fiscal year, the changes to the MD model will be documented, the model will be recalibrated, and the impact on the Room D closure predictions will be assessed.

2.5 References

Hampel, A., 2016, *Vergleich aktueller Stoffgesetze anhand von Modellberechnungen zum thermo-mechanischen Verhalten und zur Verheilung*, Tech. Report, Hampel Consulting

Hosford, W.F, 1972, A generalized isotropic yield criterion, *Journal of Applied Mechanics*, 39(2):607-609.

Munson, D. E., R. Jones, D. Hoag, and J. Ball, 1988, *Mining development test (Room D): In situ data report (March 1984-May 1988): Waste isolation pilot plant (WIPP) thermal/structural interactions program*, SAND88-1460, Sandia National Laboratories, Albuquerque, NM, USA.

Munson, D. E., A. F. Fossum, and P. E. Senseny, 1989, *Advances in Resolution of Discrepancies Between Predicted and Measured in Situ WIPP Room Closures*. SAND88-2948. Albuquerque, NM: Sandia National Laboratories.

Munson, D. E., R. Jones, C. Northrop-Salazar, and S. Woerner, 1992, *Multipass mining sequence room closures: in situ data report. Waste isolation pilot plant (WIPP) thermal/structural interactions program*, SAND87-2687, Sandia National Laboratories, Albuquerque, NM, USA, 1992.

Reedlunn, B., 2016. *Reinvestigation into Closure Predictions of Room D at the Waste Isolation Pilot Plant*. SAND2016-9961. Albuquerque, NM: Sandia National Laboratories.

3. Experimental Determination of Brucite Solubility in NaCl Solutions at Elevated Temperatures

Authors: *Leslie Kirkes* (SNL) and *Yongliang Xiong* (SNL)

3.1 Introduction

Salt formations are ideal for nuclear waste isolation, as recommended by the National Academy of Science in the 1950s (NAS 1957). The Waste Isolation Pilot Plant (WIPP) is a nuclear waste repository for US Department of Energy for disposal of defense transuranic waste in a bedded salt formation, located in southeast New Mexico. The Asse mine in Germany had been used as a research repository for radioactive waste, and is located in a domal salt formation (Schuessler et al., 2001; 2002).

In salt repositories, brucite ($Mg(OH)_2$) is influential to the near-field geochemistry. This is because crystalline MgO, which hydrates rapidly to brucite, is the only engineered barrier certified by the US Environmental Protection Agency (EPA) for the Waste Isolation Pilot Plant (WIPP) (e.g., Krumhansl et al., 2000; Xiong and Snider, 2008). An $Mg(OH)_2$-based engineered barrier is also proposed for the German Asse salt mine repository (Schuessler et al., 2001; 2002). In addition, there are several candidate repositories in salt formations, including Gorleben (Schwartz, 2012), Morsleben (Behlau and Mingerzahn, 2001; Brewitz et al., 2008) in Germany, and the sites in the Mid North Sea High and the East Midlands Shelf in the UK (Stewart, 2002). Although the engineered barrier for those candidate repositories has not been decided, MgO- or $Mg(OH)_2$-based engineered barrier would be a strong candidate. Therefore, the accurate knowledge of brucite solubilities in high ionic strength solutions at elevated temperatures is required to predict the near-field geochemical conditions of the repositories in salt formations, as brines associated with salt formations are of high ionic strength in nature.

The solubility of brucite as a function of ionic strength at room temperature has been well characterized (e.g., Xiong, 2008). However, the solubility of brucite at elevated temperatures in high ionic strength solutions, relevant to disposal of heat-generating waste in salt formations is not well known.

The objective of this work is to experimentally determine brucite solubility as a function of ionic strength in NaCl solutions up to 5.6 $mol \cdot kg^{-1}$ at elevated temperatures up to 80°C. In our work, the correction factors that are used to convert pH readings to pcH (negative logarithm of hydrogen ion concentration on a molar scale) are separately determined.

3.2 Methods

All materials (e.g., NaCl, $Mg(OH)_2$) used in this study are reagent grade from Fisher Scientific. Deionized (DI) water with 18.3 MΩ was produced by a *PURELAB Classic Water System* from ELGA. Degassed DI water was used for preparation of all starting solutions. The degassed DI water was obtained by bubbling high purity argon gas (purity 99.996%) through DI water for at least one hour, following a procedure similar to that described by Wood et al. (2002). Starting solutions were prepared such that the equilibrium solubility was approached from undersaturation with respect to brucite. The starting solutions included NaCl solutions ranging from 0.010 to 5.6 $mol \cdot kg^{-1}$ NaCl.

The experiments were conducted at five temperatures from 40 ±0.05 ºC through 80 ±0.05 ºC at an increment of 10 ºC. For each of the experiments undersaturated with respect to brucite, about 1 grams of $Mg(OH)_2$ (cr), brucite, was placed into a 150 mL high density polyethylene plastic bottle containing 100 mL of starting solution. Brucite was obtained from Fisher Scientific, and was characterized with X-ray powder diffraction (XRD) before experiments.

At specific intervals, the pH reading of each experimental solution was measured with an Orion-Ross combination pH glass electrode. Before each measurement, the pH meter was calibrated with three pH buffers (pH 4, pH 7, and pH 10) at the experimental temperature. These pH buffers were directly from

Fisher Scientific, and were traceable to NIST. In this work, the concentraction scale was adopted for the pH scale, based on correction factors as detailed below.

For solutions with ionic strengths lower than 0.10 mol·kg^{-1}, the observed solution pH readings were directly converted to hydrogen ion concentractions without a correction factor. For solutions with ionic strengths higher than 0.10 mol·kg^{-1}, the observed solution pH readings were converted to negative logarithm of hydrogen-ion concentrations (pcH) on a molar scale using a correction factor, A (see below).

The relation between the pH electrode reading (pH_{ob}) and pcH can be expressed as (Xiong et al., 2010):

$$\mathrm{pcH} = \mathrm{pH_{ob}} + A_m \tag{3.1}$$

where A_m is a pH correction factor on a molar scale. The correction factors were determined at the experimental temperatures as a function of ionic strength by following the similar procedure in Xiong et al. (2010). Then, pcH's were converted to negative logarithms of hydrogen-ion concentrations (pH_m) on a molal scale according to the following equation (Xiong et al. 2010),

$$\mathrm{pH_m} = \mathrm{pH_{ob}} + A_m = \mathrm{pH_{ob}} + A_m - \log \Theta \tag{3.2}$$

where Θ is a conversion factor from molality to molarity, which is computed from the density of a NaCl solution at the concentration and temperature of interest from Söhnel and Novotný (1985).

After each pH measurement, a solution sample was withdrawn from an experimental run. The solution was filtered using a 0.2 μm syringe filter. The filtered solution was then weighed and acidified with 0.5 mL of concentrated HNO_3 (TraceMetal grade from Fisher Scientific). The acidified solution was then diluted to 10 mL with DI water so that dissolved $\sum Mg^{2+}$ and Na^+ concentrations could be determined.

Elemental concentrations of magnesium were determined by using the Perkin Elmer Optima 8300 inductively coupled plasma atomic emission spectrometer (ICP-AES). Calibration blanks and standards were precisely matched with experimental matrices. The correlation coefficients of calibration curves in all measurements were better than 0.9995. The analytical precision is better than 1.00% in terms of the relative standard deviation (RSD) based on replicate analyses.

Phase identification for the solid phase taken from the experiments was performed by using a Bruker AXS, Inc., D8 Advance X-ray diffractometer (XRD) with a Sol-X detector. XRD patterns were collected using CuK α radiation at a scanning rate of 1.33 degrees per min for a 2θ range of 10 to 90º. The solid phase from the experiments was also characterized with electron scanning microprobe with energy dispersive spectroscopy (SEM-EDS). There is no new phase observed in those characterizations.

3.3 Experimental Results and Thermodynamic Calculations

3.3.1 Correction Factors at Elevated Temperatures as a Function of Ionic Strength

In Table 1, the experimentally determined correction factors for pH determinations in NaCl solutions at various temperatures as a function of ionic strength are listed. In addition, the correlations between correction factors and molalities of NaCl are presented as linear equations at each temperature in Table 2, based on the experimental data from Table 1.

Table 1. Experimentally determined pH correction factors at different temperatures as a function of ionic strength

Temperature [°C]	NaCl [mol·kg^{-1}]	A_M	A_m
40	1.0	0.007	–0.00469
	2.1	0.191	0.170
	3.2	0.363	0.332
	4.4	0.564	0.522
	5.6	0.762	0.708
50	1.0	–0.01	–0.0237
	2.1	0.237	0.214
	3.2	0.372	0.338
	4.4	0.579	0.535
	5.6	0.750	0.695
60	1.0	0.08	0.0641
	2.1	0.218	0.192
	3.2	0.433	0.398
	4.4	0.637	0.590
	5.6	0.758	0.700
70	1.0	0.121	0.105
	2.1	0.238	0.212
	3.2	0.429	0.394
	4.4	0.597	0.550
	5.6	0.770	0.712
80	1.0	0.124	0.103
	2.1	0.251	0.221
	3.2	0.457	0.417
	4.4	0.615	0.564
	5.6	0.713	0.651

Table 2. Concentration dependence of pH correction factors at constant temperatures

T [°C]	A_M as a function of molality	A_m as a function of molality
40	$A_M = -0.1565 + 0.1638\ m_{NaCl}$	$A_m = -0.1587 + 0.1547\ m_{NaCl}$
50	$A_M = -0.1417 + 0.1618\ m_{NaCl}$	$A_m = -0.1462 + 0.1527\ m_{NaCl}$
60	$A_M = -0.07746 + 0.1542\ m_{NaCl}$	$A_m = -0.08406 + 0.1451\ m_{NaCl}$
70	$A_M = -0.03886 + 0.1441\ m_{NaCl}$	$A_m = -0.04546 + 0.1351\ m_{NaCl}$
80	$A_M = -0.004252 + 0.1338\ m_{NaCl}$	$A_m = -0.01614 + 0.1249\ m_{NaCl}$

3.3.2 Solubility of Brucite in NaCl Solutions at Elevated Temperatures

In Table 3, the raw experimental data concerning solubility of brucite in NaCl solutions at elevated temperatures are tabulated. The total magnesium concentrations from solubility of brucite are related to the following reactions,

$$Mg(OH)_2(cr) + 2H^+ \rightleftharpoons Mg^{2+} + 2H_2O(l) \quad (3.3)$$

$$Mg^{2+} + H_2O(l) \rightleftharpoons MgOH^+ + H^+ \quad (3.4)$$

In this work, we compute the equilibrium quotients for Reaction (3.3), Q_{s2}, based on our solubility data. The free magnesium concentrations, $m_{Mg^{2+}}$, are calculated from our measured total magnesium concentrations and corrected pH values after calculating equilibrium concentration of $MgOH^+$, m_{MgOH^+}, using total Mg species mass-balance Equation 3.5 and the equilibrium quotients for Reaction (3.4), $Q_{1,1}$, from Palmer and Wesolowski (1997) in NaCl solutions at the respective temperatures and ionic strengths,

$$m_{\Sigma Mg} = m_{Mg^{2+}} + m_{MgOH^+} \tag{3.5}$$

$$Q_{1,1} = \frac{m_{MgOH^+} \cdot m_{H^+}}{m_{Mg^{2+}}} = \frac{\left(m_{\Sigma Mg} - m_{Mg^{2+}}\right) m_{H^+}}{m_{Mg^{2+}}} \tag{3.6}$$

Therefore, using the experimentally determined total magnesium and corrected hydrogen ion concentrations, free magnesium concentrations can be determined by solving Eq. (3.6) for $m_{Mg^{2+}}$. After obtaining $m_{Mg^{2+}}$, equilibrium quotients for Reaction (3.3) can be computed. The equilibrium quotients for Reaction (3.3) determined in this study are tabulated in Table 3.

Using the specific ion interaction theory (SIT) coefficients, $\varepsilon(Mg^{2+}, Cl^-)$ and $\varepsilon(H^+, Cl^-)$, from Xiong (2006), at the experimental temperatures of this work, the equilibrium quotients in Table 3 are extrapolated to infinite dilution. The equilibrium constants for Reaction (3.3) for each temperature at infinite dilution are listed in Table 4.

Table 3. Equilibrium quotients for Reaction (3.3) determined in this study

T [°C]	m_{NaCl} [mol·kg^{-1}]	$\log Q_{s2} \pm 2\sigma$
40	0.010	16.57 ± 0.09
	0.10	16.85 ± 0.09
	1.0	16.92 ± 0.15
	2.1	17.07 ± 0.13
	3.2	17.03 ± 0.25
	4.4	17.15 ± 0.27
	5.6	17.23 ± 0.22
50	0.010	16.17 ± 0.16
	0.10	16.46 ± 0.33
	1.0	16.42 ± 0.17
	2.1	16.63 ± 0.30
	3.2	16.51 ± 0.61
	4.4	16.64 ± 0.32
	5.6	16.74 ± 0.38
60	0.010	15.74 ± 0.18
	0.10	15.88 ± 0.18
	1.0	16.11 ± 0.25
	2.1	16.17 ± 0.27
	3.2	16.37 ± 0.21
	4.4	16.56 ± 0.32
	5.6	16.51 ± 0.31
70	0.010	15.21 ± 0.15
	0.10	15.39 ± 0.15
	1.0	15.60 ± 0.20
	2.1	15.70 ± 0.28
	3.2	15.81 ± 0.27
	4.4	15.97 ± 0.38
	5.6	16.13 ± 0.24
80	0.010	14.89 ± 0.20
	0.10	15.02 ± 0.29
	1.0	15.24 ± 0.26
	2.1	15.54 ± 0.06
	3.2	15.64 ± 0.20
	4.4	15.79 ± 0.29
	5.6	15.79 ± 0.37

Table 4. Equilibrium constants for Reaction (3.3) at infinite dilution determined in this work

T [°C]	$\log K_{s2}^{0} \pm 2\sigma$
40	16.43 ± 0.22
50	15.96 ± 0.32
60	15.63 ± 0.11
70	15.12 ± 0.08
80	14.84 ± 0.16

3.4 Conclusions

In this study, we have determined the solubility constants of brucite in NaCl solution at elevated temperatures up to 80 ºC. The hydrogen ion concentrations in our experiments in NaCl solutions to high ionic strength at elevated temperatures are determined by applying the correction factors that are experimentally acquired in this work. As brines associated with salt formations are of high ionic strength in nature, the results from our work are highly applicable to nuclear waste isolation in salt formations.

3.5 References

Behlau, J. & G. Mingerzahn, 2001. Geological and tectonic investigations in the former Morsleben salt mine (Germany) as a basis for the safety assessment of a radioactive waste repository. *Engineering Geology,* 61(2):83–97.

Brewitz, W., J. Droste & G. Stier-Friedland, 2008. Geological features of the Morsleben repository and their relevance for long-term safety. *Reviews in Engineering Geology*, 19:53 66.

Krumhansl, J.L., H.W. Panenguth, P.-C. Zhang, J.W. Kelly, H.L. Anderson & J.O. Hardesty, 2000. "Behavior of MgO as a CO_2 scavenger at the Waste Isolation Pilot Plant (WIPP), Carlsbad, New Mexico". *Materials Research Society Symposium Proceedings*, 608:155-160.

NAS (US National Academy of Sciences Committee on Waste Disposal), 1957. *The Disposal of Radioactive Waste on Land*. Publication 519. Washington, DC: National Academy of Sciences–National Research Council.

Palmer, D.A. & D.J. Wesolowski, 1997. Potentiometric measurements of the first hydrolysis quotient of magnesium (II) to 250 ºC and 5 molal ionic strength (NaCl). *Journal of Solution Chemistry* 26(2):217-232.

Schuessler, W., B. Kienzler, S. Wilhelm, V. Neck & J.I. Kim, 2001. "Modeling of Near Field Actinide Concentrations in Radioactive Waste Repositories in Salt Formations: Effect of Buffer Materials" in *Materials Research Society Symposium Proceedings*, 663:791.

Schüssler, W., V. Metz, B. Kienzler & P. Vejmelka, 2002. Geochemically based source term assessment for the Asse salt mine: comparison of modeling and experimental results (Abstract). *Programs and Abstracts of Materials Research Society Annual Meeting at Boston, MA*, p. 713.

Schwartz, M.O., 2012. Modelling groundwater contamination above a nuclear waste repository at Gorleben, Germany. *Hydrogeology Journal*, 20(3):533-546.

Söhnel, O. & P. Novotný, 1985. *Densities of Aqueous Solutions of Inorganic Substances*. Elsevier, New York, 335 p.

Stewart, S., 2002. Exploring the continental shelf for low geological risk nuclear waste repository sites using petroleum industry databases: a UK case study. *Engineering Geology*, 67(1):139-168.

Wood, S.A., D.A. Palmer, D.J. Wesolowski & P. Bénézeth, 2002. "The aqueous geochemistry of the rare earth elements and yttrium. Part XI. The solubility of $Nd(OH)_3$ and hydrolysis of Nd^{3+} from 30 to 290 ºC at saturated water vapor pressure with in-situ pH_m measurement" in Hellmann, R. & S.A. Wood [Eds], *Water-Rock Interactions, Ore Deposits, and Environmental Geochemistry: A Tribute to David Crerar*, Special Publication 7, The Geochemical Society, pp. 229-256.

Xiong, Y.-L., 2006. Estimation of medium effects on equilibrium constants in moderate and high ionic strength solutions at elevated temperatures by using specific interaction theory (SIT): interaction coefficients involving Cl^-, OH^- and Ac^- up to 200 ºC and 400 bars. *Geochemical Transactions*, 7(1):4.

Xiong, Y.-L., 2008. Thermodynamic properties of brucite determined by solubility studies and their significance to nuclear waste isolation. *Aquatic Geochemistry*, 14(3):223-238.

Xiong, Y.-L. & A.C.S. Lord, 2008. Experimental investigations of the reaction path in the $MgO–CO_2–H_2O$ system in solutions with ionic strengths, and their applications to nuclear waste isolation. *Applied Geochemistry,* 23:1634-1659.

Xiong, Y.-L., H. Deng, M. Nemer & S. Johnsen, 2010. Experimental determination of the solubility constant for magnesium chloride hydroxide hydrate ($Mg_3Cl(OH)_5·4H_2O$, phase 5) at room temperature, and its importance to nuclear waste isolation in geological repositories in salt formations. *Geochimica et Cosmochimica Acta*, 74:4605-4611.

4. Dissolution of Borosilicate Glass into Brine Solutions

Authors: *Jonathan P. Icenhower* (SNL) and *Yongliang Xiong* (SNL)

4.1 Introduction

International consensus has converged on borosilicate glass as a matrix for immobilizing certain kinds of nuclear waste. Hanford tank waste, for example, will be mixed with a boron-bearing material called "frit" and melted. After it is poured into a steel canister, the molten material cools and solidifies as glass, and the radionuclide elements are structurally bonded to other elements within the vitreous network and effectively immobilized. The glass waste form can then be disposed in a deep geologic repository where it will be a chemically durable waste form. Because of the benefits that boron imparts to silicate glass, such as lowering melt viscosity and melting temperature, borosilicate glass is the preferred chemical composition for an immobilization matrix. However, borosilicate glass is moderately vulnerable to aqueous attack and, if brine solution intrudes the repository and breaches the canisters, dissolution will occur, releasing radionuclides to solution. The rate at which borosilicate glass, and thereby the radionuclide elements, dissolves into brine solution determines, in part, the radionuclide source-term in a geologic repository.

Despite decades of research and experimentation that bears on glass reactivity, relatively few investigations have been carried out on quantifying dissolution kinetics in brine solutions. Abdelouas et al. (1995), Grambow & Strachan (1983), Grambow & Müller (1989), Grambow et al. (1994), Luckscheiter & Nesovic (1997), McGrail et al. (1986), Pederson et al. (1993), Strachan (1983), Strachan et al. (1984) and Zimmer et al. (2002) reported results from experiments on the reactivity of borosilicate glass in a variety of NaCl- and $MgCl_2$-based solutions. To summarize the results, Pederson et al. (1993) found that although rates of sodium and hydrogen interdiffusion did not increase with higher concentrations of sodium in the brine solution, the presence of magnesium in typical brines increased the dissolution rate of borosilicate glass. Strachan (1983) and Strachan et al. (1984) proposed that the presence of magnesium increased rates of glass corrosion by forming Mg-silicates on the surface of the reacting samples. Formation of magnesium silicates affects glass dissolution rates because more silica from dissolution goes into solution to counter the silica that goes into making phases such as sepiolite (an Mg-rich phyllosilicate). An additional reason that Mg increases glass dissolution rates can be found in Grambow & Müller (1989) and Grambow et al. (1994). They proposed that solution pH decreased in Mg-brines because formation of Mg-rich phyllosilicates produces H^+ through the reaction:

$$2Mg^{2+} + 3H_4SiO_4 = Mg_2Si_3O_6(OH)_4 + 2H_2O + 4H^+ \quad (4.1)$$

Previous investigations indicate that this reaction will govern the solution pH until most of the Mg^{2+} is consumed, after which the solution pH will "rebound" back up to neutral to slightly alkaline values (Grambow & Müller 1989). On the other hand, dissolution of borosilicate glass into NaCl brine solutions causes the solution to increase in pH through the precipitation of Na-rich zeolites. Under alkaline conditions, the presence of Na^+ in solution catalyzes the formation of zeolites, and causes additional release of hydroxyl to solution:

$$2Na^+ + 3[H_4SiO_4]^- + 2[Al(OH)_4]^- = Na_2[Al_2Si_3O_{10}]\cdot 2H_2O + 3OH^- + 5H_2O \quad (4.2)$$

Reactions that result in strongly acidic or alkaline solutions will have a deleterious effect on glass dissolution, with concomitant faster release of radionuclides. However, previous studies have not yet worked out which of these pH-affecting reactions will dominate in typical Na-Mg-Cl brines, the length of time needed for a pH excursion to occur, and the timing of the "rebound" to more moderate pH conditions. Accordingly, the lack of a systematic examination of the effects of ionic strength or brine constituent identity on dissolution hampers our ability to predict how borosilicate glass waste forms may

react in a salt repository. Therefore, this work addresses these issues and seeks to furnish quantitative dissolution rate date for borosilicate glass reactions in sodium and magnesium chloride-bearing brines.

4.2 Experimental Process Description

4.2.1 Overall Strategy and Process

In order to unravel the various mechanisms that govern glass dissolution reactions, both flow-through and static dissolution experiments were conducted. These two types of tests have different purposes and, when carried out in conjunction with each other, can produce a set of data from which powerful insights can be drawn. The objective of flow-through experiments is to parameterize the rate equation, such that the glass dissolution rate for any set of conditions can be quantified. The rate equation is expressed as:

$$\text{rate} = k_{\circ} S \exp\left(\frac{-E_a}{RT}\right) a_{H^+}^{\eta_{H^+}} g(I) f(\Delta G_r) \prod_i a_i^{n_i} \qquad (4.3)$$

where $k_{\circ}$ is the rate constant, S is the sample surface area, E_a is the experimental activation energy, a is the activity of the subscripted species, η is the activity power law coefficient, $g(I)$ is a term expressing the rate dependence upon solution ionic strength, $f(\Delta G_r)$ is a term expressing the rate dependence upon departure from equilibrium, $\prod_i a_i^{n_i}$ represents the dependence of the rate upon any catalyzing or rate inhibiting species, and R and T are, respectively, the gas constant and temperature on the kelvin scale. By holding some parameters constant while varying others, an investigator can fully parameterize the rate equation for a specific glass composition. An example of how this can be used in the present set of experiments is in de-convoluting the effects of Mg^{2+} on the dissolution rate. In the previous section, it was noted that Mg^{2+} affects dissolution rates when silica released from glass dissolution forms Mg-silicates, causing the glass to dissolve more rapidly in compensation. The formation of Mg-silicates, primarily phyllosilicates, also results in a decrease in pH (Eq. 4.1). By conducting flow-through experiments with a constant input of Mg^{2+} in pH-buffered solution, the dissolution rate will occur at a constant pH value, so the effects of silica sequestration into phyllosilicates can be quantified. Once the dissolution kinetics as a function of Mg^{2+} concentration have been mapped out, then static experiments can be used to show how changes in pH, through production of hydronium (Eq. 4.1), affect rates.

Static experiments derive their name from the lack of refreshment of reactant (or "leach") solution over the duration of the experiments (thus, the solution is "static" and non-circulating). The purpose of static experiments is to elucidate how changes in solution chemistry (including pH) over time affect the dissolution behavior of glass. Static experiments also have the added benefit of stabilizing secondary phases, such as the Mg-rich phyllosilicates and Na-rich zeolites, whose abundance and chemical compositions are important pieces of the puzzle. The other objective of static experiments is to obtain static-state compositions to provide the insight into the local/global equilibrium with respect to the glass corrosion. This would provide important data for both kinetic and thermodynamic modeling.

The two types of experiments are discussed in more detail below.

4.2.1.1 Single-Pass Flow-Through (SPFT) Experiments

Single-Pass Flow-Through (SPFT) experiments are designed to determine dissolution rates at constant solution compositions. When the solid sample reacts with water, the concentrations of elements released into solution are limited by the rate of fluid flow. Therefore, a condition of "dynamic equilibrium" or "steady-state" develops in which the concentrations of elements at the output are constant with respect to time. When the flow-rate is set properly, the pH of solution will also be constant over the duration of the experiment. In this way, the effects of solution composition on dissolution rates can be unraveled from pH change effects.

In a typical flow-through dissolution experiment, powdered samples of the test material are placed into a reactor and solution, at a set chemical composition and temperature, flows through the reactor. The glass dissolves into solution and the elements released are measured in the effluent in collection vials (see Figure 1). The concentrations of elements at a known flow rate in glass of a measured chemical composition and surface defines the dissolution rate of the glass. In the form of an equation, the dissolution rate is:

$$\text{rate} = \frac{(c_{i,j} - \bar{c}_{i,b})q_j}{f_i S_j m} \tag{4.4}$$

where $c_{i,j}$ is the concentration of element i at time j (mol/kg), $\bar{c}_{i,b}$ is the average background concentration of element i (mol/kg), q_j is the flow-rate at time j (kg/s), f_i is the mole fraction of element i in the sample (dimensionless), S_j is the surface area of the sample (m^2/kg), and m is the mass of the sample (kg). Typically, one chooses the element boron as the index of dissolution because its release from glass is proportional to the rate of glass dissolution and because boron does not form secondary phases in the corrosion layer that forms on the sample surface. In the case in which the inflowing solution is dilute, determining the concentration of boron in the effluent solution is easily accomplished using ICP-AES or –MS methods. However, when solutions are not dilute, as for the case in which brine solutions are used, quantifying the concentration of boron in solution becomes more difficult. ICP analysis methods typically necessitate that solutions be dilute with respect to NaCl and similar components of brine solutions, and therefore require that effluent solutions undergo dilution. Accordingly, as brine solutions become more concentrated, the degree of dilution must also increase, making analysis of elements like boron more challenging and increasing experimental uncertainty. To overcome this experimental difficulty, we used an interferometric method to determine dissolution rates.

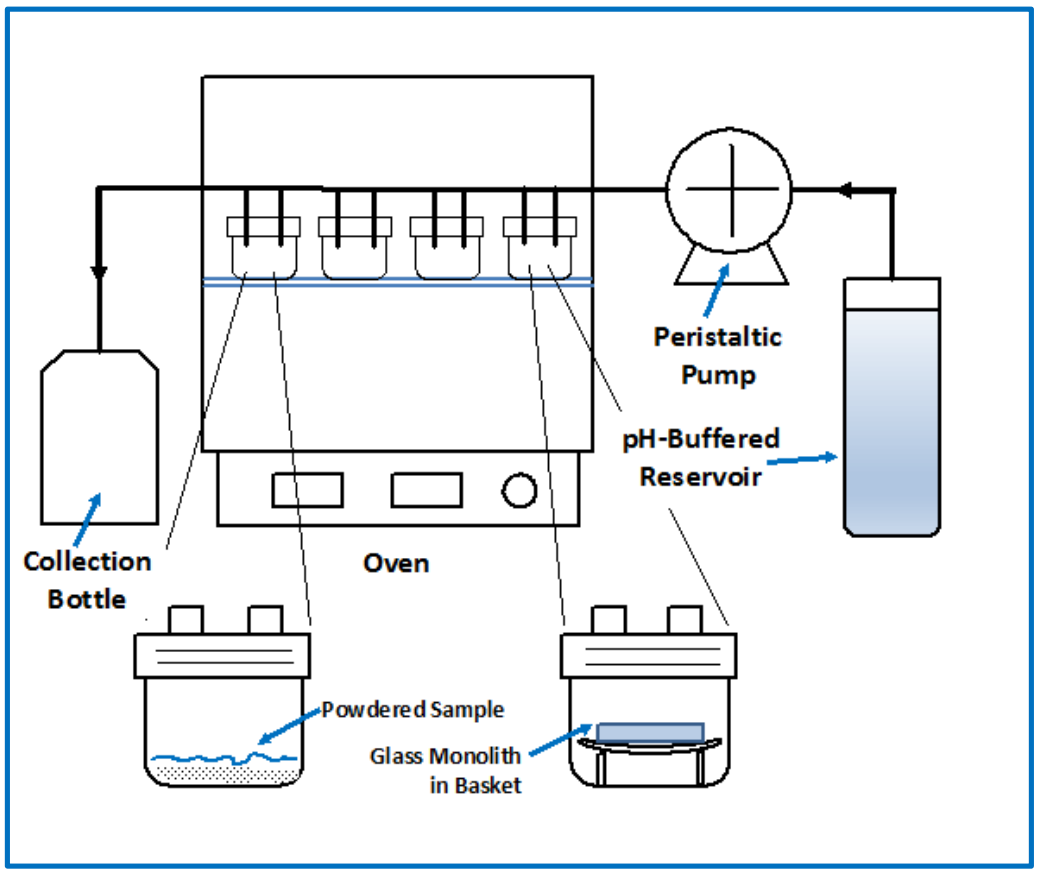

Figure 1. Schematic of the Single-Pass Flow-Through (SPFT) system

The interferometry technique uses the difference in the phase shift in light when a beam of light reflects from the surface of a sample. Commercial interferometers are essentially microscopes in which a Mirau objective has been placed in the light beam path. White light is split by the Mirau objective into two separate beams, one that reflects off the sample surface, the other serving as a reference. A difference in path length between the two beams will result in constructive and destructive interferences that are manifested as light and dark "fringes" on the sample surface. As the light source moves vertically with respect to the sample surface, a series of fringes will appear and a CCD camera will record the pattern and software will interpret the pattern in terms of vertical height difference. The software can then construct a three-dimensional height map over the scanned area (typically over a several micrometer-by-micrometer area) with detectable vertical height differences of <2 nanometers (depending on the objectives used). Figure 2 illustrates the concepts of interferometry.

Dissolution studies can take advantage of the instrument's ability to detect minute height differences in the following way. Instead of using powdered samples, monolithic (in this case, a glass coupon with dimensions of ~2 × 2 × 0.40 cm) samples were used. A small bead of waterproof adhesive that acts to prevent water from reacting with a small portion of the glass was placed on the well-polished surface. Glass coupons with masked areas were placed into a flow-through reactor and then removed after a period of time. During exposure to solution, the unmasked portion of the glass dissolved, resulting in surface retreat. The adhesive mask was removed, leaving behind a preserved "reference" surface against which surface retreat of the exposed portion of the glass was measured. A cartoon illustrating the relationship between the mask and the reference and reacted surfaces is shown in Figure 3. The height difference between the reference and reacted surface is proportional to the dissolution rate of the glass:

$$\text{rate} = \frac{\rho \Delta h}{\Delta t} \tag{4.5}$$

where ρ is the glass density (g/m^3), Δh is the difference in height between the reference and reacted surfaces (m), and Δt is the elapsed time of the experiment (s). Note that the rate calculated in Eq. (4.2) is in units of g/(m^2·s), which is easily converted into mol/(m^2·s).

The advantage of using interferometry is that rates were determined rapidly, accurately, and without resorting to large degrees of effluent solution dilution. All that is required is a flat, light reflective surface that can be imaged with the interferometer. Even for a small "spot" preserved as a reference surface, dozens of height measurements were performed around the perimeter.

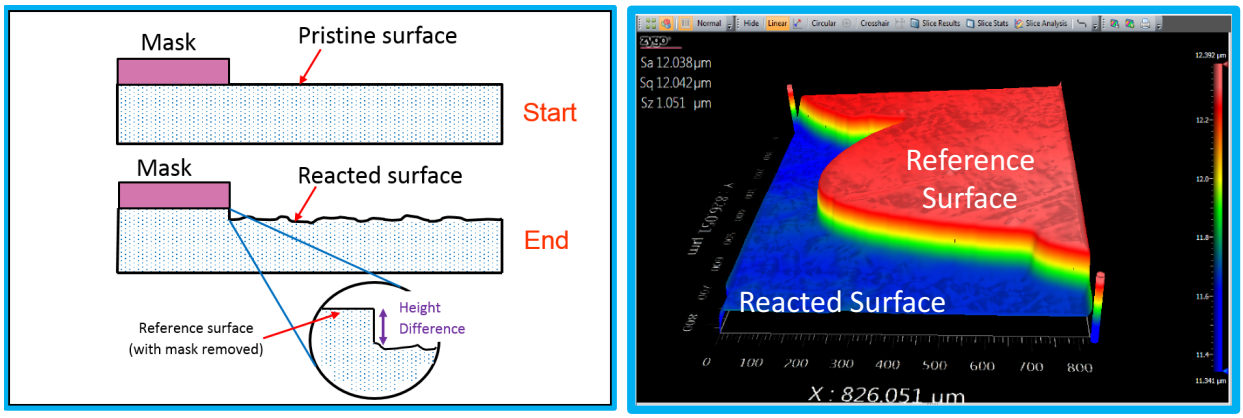

Figure 2. Left (A): Cartoon of interferometric technique for determining glass monolith dissolution rates. Right (B): A three-dimensional height map of a portion of the reference and reacted surfaces of a glass monolith exposed to solution at 90°C

4.2.1.2 Static Experiments

In static experiments, glass powders with a known surface area were placed in reactors with a set amount of solution. Unlike flow-through experiments, in which concentration of species in solution are maintained at constant values, the concentration of elements released from glass increase with time until precipitation of one (or more) secondary phase(s) occurs. In this context, the formation of a set of phases is more important than obtaining rate data from the solution chemistry. The main use of static experiments is to document the paragenetic sequence of phases that are produced in static experiments and then deduce the reaction path of the glass over time. In addition, if the solution is not strongly pH-buffered, the pH of the solution will also change over time, as H^+ or OH^- are consumed or produced by reaction. Because the large change in solution pH anticipated in brine solutions, and hence the increase in glass dissolution rate, the evolution of pH will an important value to track. Such experiments depend, in part, on the relative masses of solids and solutions in the experiment.

4.3 Materials

The glass that was used in the experiments, the "International Simple Glass" or ISG, is a six-component composition in the system Al-B-Ca-Na-Si-Zr. Table 5 lists its chemical composition.

Table 5. Chemical composition of ISG glass in mole % and weight % oxides.

Oxide	Mole %	Weight %
SiO_2	60.2	56.2
B_2O_3	16.0	17.3
Al_2O_3	3.8	6.1
Na_2O	12.6	12.2
CaO	5.7	5.0
ZrO_2	1.7	3.3
Total	100.0	100.0

Glass monoliths were polished to 0.3 µm grit to produce a flat, mirror-like reflective surface that were conducive for imaging by interferometry.

4.4 Results

4.4.1 Single-Pass Flow-Through (SPFT)

4.4.1.1 NaCl Solutions

Figure 3 illustrates, through the release of Si from glass to solution, that the glass/water system comes to steady-state conditions in ~30 to 50 days in NaCl solutions. Concentrations plotted in Figure 3 are measured Si from the effluent solution by ICP-AES. From measured release of Si we calculated rates (equation 4.4) and then compared them to rates measured by interferometry (equation 4.5).

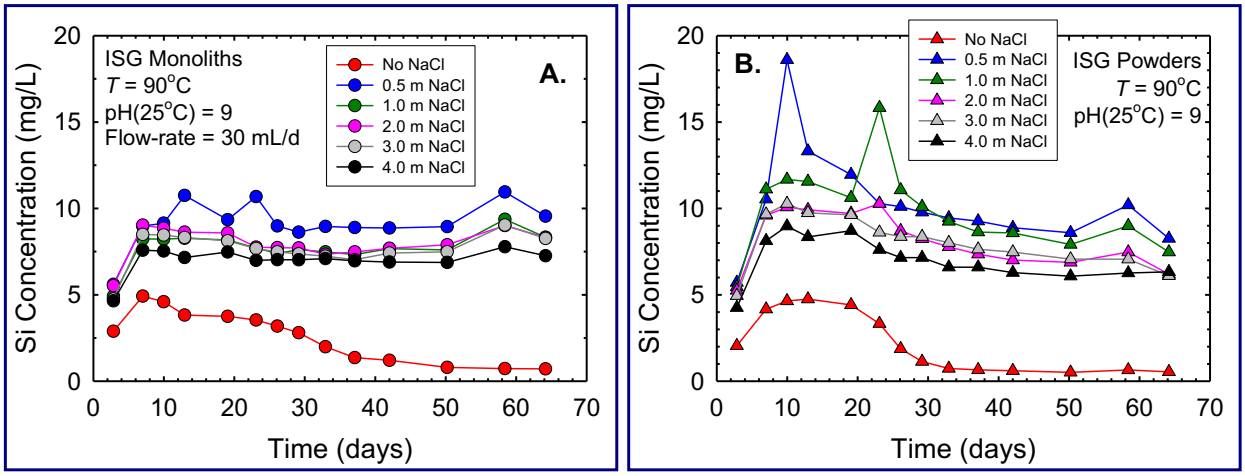

Figure 3. Approach to steady-state conditions for monoliths (A left) and powders (B right). The figures show the release of Si from glass to solution

Figure 4 indicate the release of Si from glass to solution is slowest for the solution that contains no NaCl, is fastest for the 0.5 molal NaCl solutions, then progressively decreases with increasing NaCl. Calculated dissolution rates were consistent with: the presence of even low concentrations of NaCl increases the dissolution rate of borosilicate glass.

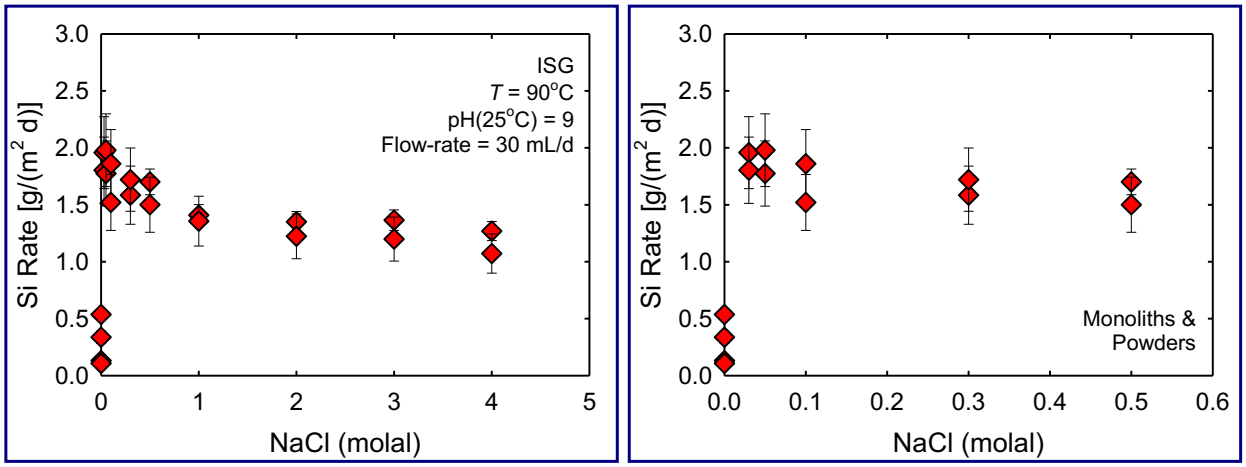

Figure 4. (A left) Dissolution rate (based on measured Si release to effluent) versus NaCl for both monoliths and powders. (B right) Dissolution rate versus NaCl up to 0.6 m illustrating the effect of NaCl on borosilicate glass.

The data suggest that NaCl causes an increase in the rate of borosilicate glass dissolution, just as in the case of SiO_2 polymorphs; Na^+ plays an indirect (i.e., catalysist) role in the observed increase in silica polymorph reaction rates (Dove, 1999; Icenhower & Dove, 2000).

To determine relationship between NaCl and the rate, we normalized the dissolution rates by dividing the rates in NaCl-bearing solutions by the average rate in NaCl-free solutions. In this way, we could compare rates between SiO_2 polymorphs and borosilicate glass on a more-or-less even basis as shown in Figure 5:

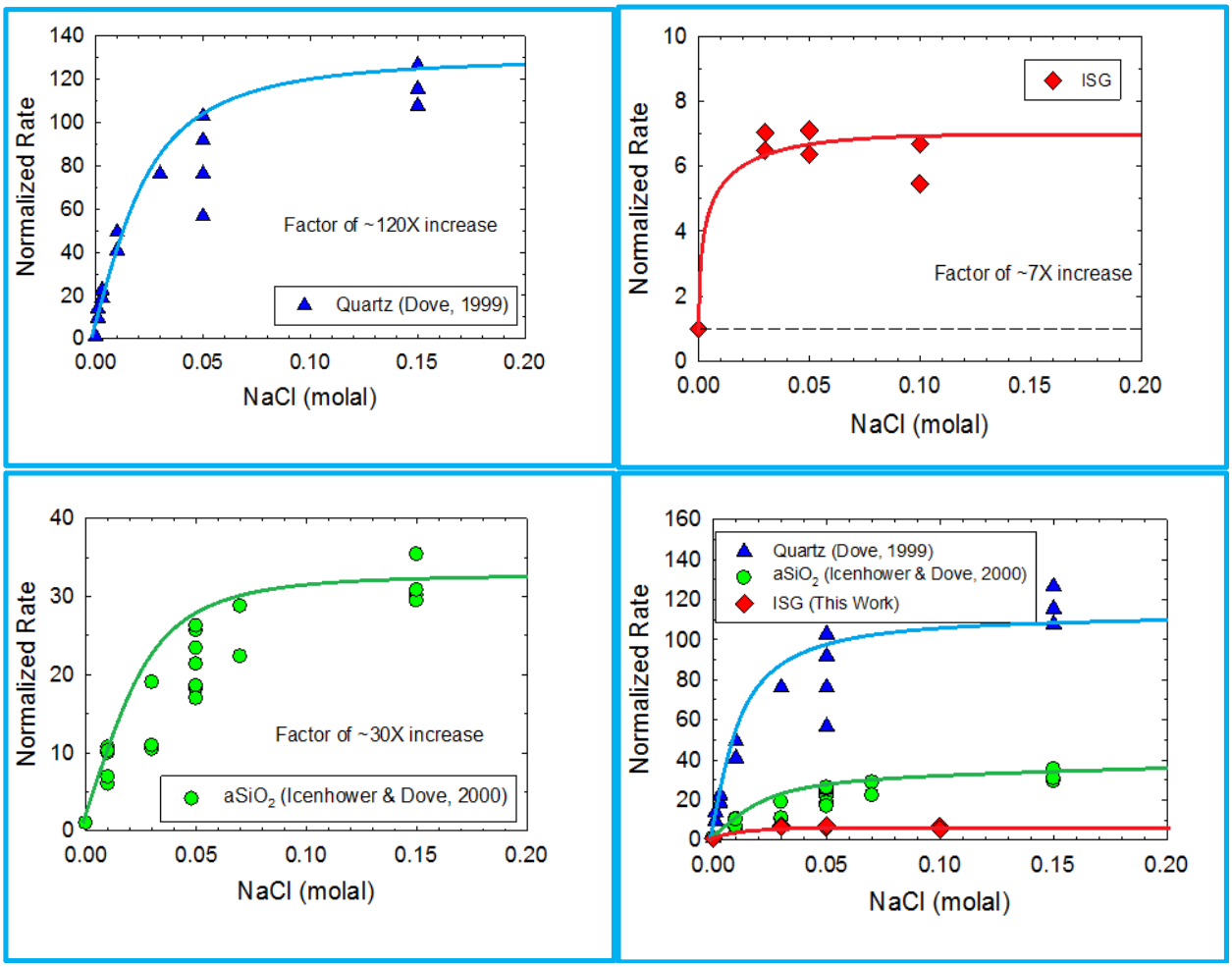

Figure 5. Normalized Rates (rates in NaCl solutions/average rates in NaCl-free solutions) versus NaCl for (A top left) β-quartz, (B bottom left) $aSiO_2$ (amorphous silica), (C top right) ISG borosilicate glass (this work), and (D bottom right) all three solids on the same plot.

As Figure 5 illustrates, the dissolution behavior of ISG glass is similar to that of the silica polymorphs, even though the magnitude of the rate enhancement is not as large. These data suggest that silica polymorphs and borosilicate glass dissolution is governed by breaking of Si—O bonds.

With increasing NaCl in solution, Figure 6 illustrates that the rates decrease from peak values in a linear fashion:

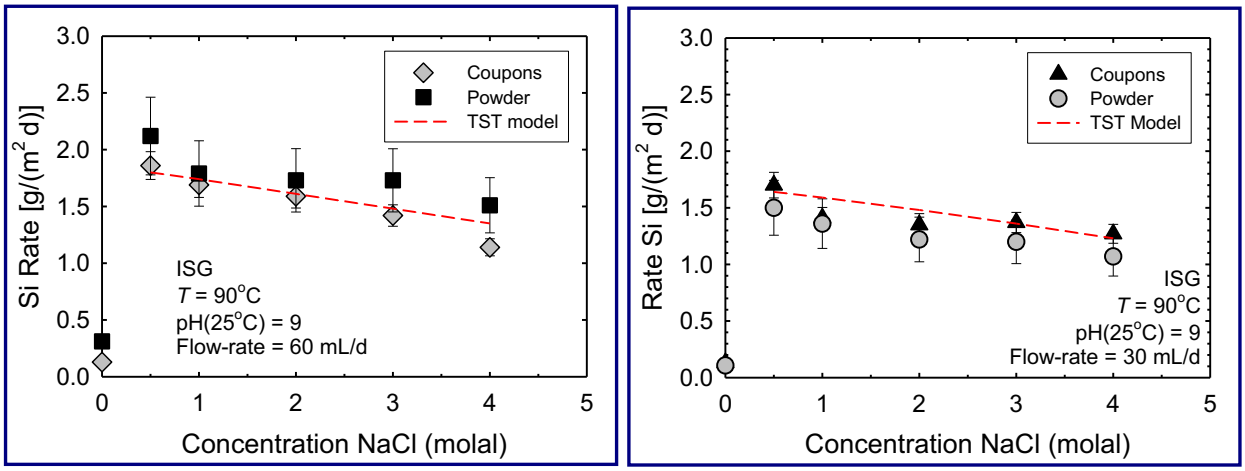

Figure 6. Dissolution rate (based on Si release) versus NaCl concentration. Rates for monoliths and powders are distinguished. The data suggest that the dissolution rate in concentrated brines is governed by the decrease in the activity of water

These data can be understood in terms of the model for silica dissolution:

$$\text{rate} = k_0 \cdot \left(a_{SiO_2}\right) \cdot \left(a_{H_2O}\right)^2 \cdot \left(1 - \frac{Q}{K}\right) \quad (6)$$

This rate expression indicates that the rate is a product of k_0, the rate constant [g/(m^2·d)], the activity of silica in the glass (dimensionless), the activity of water (dimensionless) and a term describing the departure from equilibrium $\left(1 - \frac{Q}{K}\right)$ (dimensionless and ~1 for SPFT tests as solution composition is maintained constant and far from equilibrium, i.e., Q/K ~0). Thus, the decrease in the activity of water, occurring in response to the increase of NaCl in solution, results in a rate decrease. This relationship can be understood in terms of Transition State Theory (TST); there are fewer free molecules of water available that can rupture the Si—O bond.

4.4.1.2 $MgCl_2$ & Mixed (NaCl-$MgCl_2$) Solutions

Dissolution rates for ISG were determined by Si release. Because Si concentrations in the effluent approach the analytical quantification limit, rates were also determined using interferometry. The rates are very similar (~4× difference maximum). As Figure 7 demonstrates, the rates of borosilicate glass dissolution decrease as Mg is added to solution.

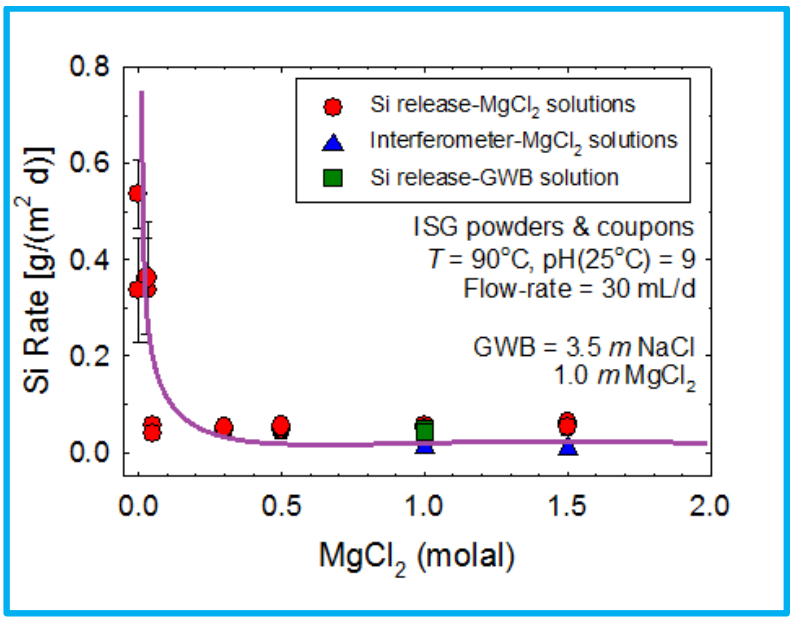

Figure 7. Dissolution rate versus $MgCl_2$ concentration. Rates were determined by Si assay in $MgCl_2$ (red circles), in simplified synthetic brine (GWB; green squares) and by interferometry (blue triangles). Powders and monoliths are not differentiated on this figure. Note that the dissolution rate of ISG in the synthetic GWB is indistinguishable from the rates in $MgCl_2$ only.

The difference in dissolution rates between glass reacted in NaCl versus $MgCl_2$ is shown in Figure 8. The maximum and minimum differences are ~70 and 40 times. In addition, note that the rate of the glass reacted in the simple brine (GWB; 3.5 m NaCl, 1.0 m $MgCl_2$) is indistinguishable from glass reacted in $MgCl_2$ only. These data demonstrate that the effects of Mg^{2+} dominate over those of Na^{+}.

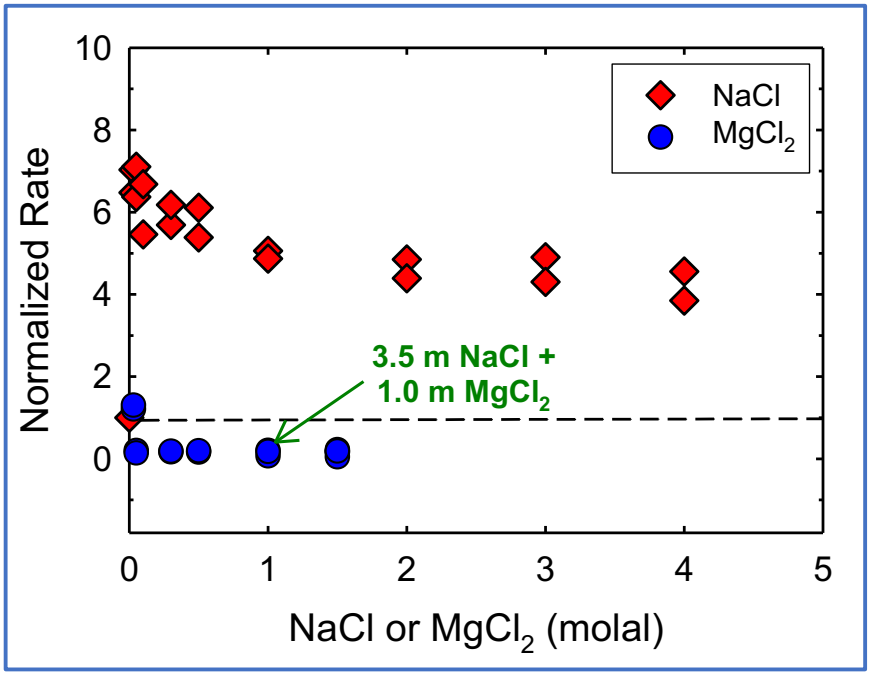

Figure 8. Normalized dissolution rate versus concentration of either NaCl or $MgCl_2$

4.4.2 Static Experiments

As of August 2017, we have terminated the static experiments, which have been running for nearly one year. The solution pH is being measured and an aliquot of solution is being set aside for ICP-AES analysis. The remaining solids will be rinsed and dried and will be examined to determine if secondary corrosion products have formed. Specifically, an aliquot of the powders will be mounted on a stub and examined by Scanning Electron Microscopy (SEM) and another aliquot will be ground and made into an X-Ray Diffraction (XRD) mount. The results of these analyses will be reported in the paper that we will submit for publication in a peer-reviewed journal.

4.5 Conclusions

The conclusions stated here are preliminary and may be subject to modifications once all the data are collected. The current data suggest that addition of even low concentrations of NaCl to solution enhances the dissolution rate of borosilicate glass. This behavior is similar to that observed for the SiO_2 polymorphs (β-quartz and amorphous silica). The similarity in behavior argues that the principal mechanism by which multicomponent borosilicate glass dissolves is by rupture of the Si—O bond. At higher concentrations of NaCl the rates decrease, due to a decrease in the activity of water. The presence of $MgCl_2$ inhibits glass dissolution in flow-through reactors. A different behavior might occur in static reactors, in which Mg-rich clay minerals are likely to form. Clay minerals could form in flow-through reactors, but at the flow-rates used in these experiments, the concentration of key clay constituents, such as Si and Al, are probably too low to saturate clays. Experiments conducted in static reactors, in which clay minerals should form, have not yet been analyzed. The results of our experiments will be reported in an article submitted to a peer-reviewed journal.

4.6 References

Abdelouas, A., J.L. Crovisier, W. Lutze, R. Müller & W. Bernotat, 1995. Structure and chemical-properties of surface-layers developed on R7T7 simulated nuclear waste glass altered in brine at 190 ºC. *European Journal of Mineralogy*, 7:1101-1113.

Dove, P. M. (1999) The dissolution kinetics of quartz in aqueous mixed cation solutions. *Geochimica et Cosmochimica Acta* 63(22):3715-3727.

Grambow, B. & D. Strachan, 1983. “Leach testing of waste glass under near-saturation conditions” in: McVay [Ed], *Scientific Basis for Nuclear Waste Management VII*. Elsevier Science Publication Co, New York, NY, pp. 623-634.

Grambow, B. & R. Müller, 1989. “Chemistry of glass corrosion in high saline brines” in: Oversby & Brown [Eds], *Scientific Basis for Nuclear Waste Management XIII,* Materials Research Society, Pittsburgh, PA, pp. 229-240.

Grambow, B., A. Loida, L. Kahl & W. Lutze, 1994. “Behavior of Np, Pu, Am, Tc upon glass corrosion in a concentrated $Mg(Ca)Cl_2$ solution” in: Murakami & Ewing [Eds], *Scientific Basis for Nuclear Waste Management XVIII*, Materials Research Society, Pittsburgh, PA, pp. 39-46.

Icenhower, J.P. & P.M. Dove, 2000. The dissolution kinetics of amorphous silica into sodium chloride solutions: Effects of temperature and ionic strength. *Geochimica et Cosmochimica Acta* 64(24):4193-4203.

Icenhower, J.P. & C.I. Steefel, 2015. Dissolution rate of borosilicate glass SON68: A method of quantification based upon interferometry and implications for experimental and natural weathering rates of glass. *Geochimica et Cosmochimica Acta,* 157:147-163.

Luckscheiter & Nesovic, 1997. Long term corrosion behavior of the WAK-HLW glass in salt solutions. *Waste Management*, 17(7):429-436.

McGrail, B.P., L.R. Pederson & D.A. Petersen, 1986. The influence of surface potential and pH on the release of sodium from $Na_2O \cdot 3SiO_2$ glass. *Physics and Chemistry of Glasses*, 27(2):59-64.

Pederson, L.R., B.P. McGrail, G.L. McVay, D.A. Petersen-Villalobos & N.S. Settles, 1993. Kinetics of alkali silicate and aluminosilicate glass reactions in alkali chloride solutions: Influence of surface charge. *Physics and Chemistry of Glasses*, 34(4):140-148.

Strachan, D.M., 1983. Results from long-term use of the MCC-1 static leach test method. *Nuclear and Chemical Waste Management,* 4(2):177-188.

Strachan, D.M., K.M. Krupka & B. Grambow, 1984. Solubility interpretations of leach tests on nuclear waste glass. *Nuclear and Chemical Waste Management,* 5(1):87-99.

Zimmer, P., E. Bohnert, D. Bosbach, J.I. Kim & E. Althaus, 2002. Formation of secondary phases after long-term corrosion of simulated HLW glass in brine solutions at 190 ºC. *Radiochimica Acta,* 90(9-11):529-535.

5. Partitioning of Fission Products (Cs, Sr, and I) into Salt Phases

Author: *Jonathan P. Icenhower* (SNL)

5.1 Introduction

Evaporite salt deposits are well distributed throughout the world, including major deposits in North America, Asia, Europe, South America, the Near East and Central Asia. Although halite is commonly the major constituent of evaporate deposits, other phases, such as gypsum, anhydrite and a host of potassium and magnesium minerals are typically abundant. These deposits have been mined for centuries as a source of salt and, more recently, as a source of potassium for fertilizer. A recent development in subsurface salt mining has been the realization that salt deposits can be used as a host rock for deep geologic disposal of radioactive waste (Pierce & Rich 1962). This viewpoint is based on the qualities of self-sealing, low permeability and high thermal conduction of salt.

In the Southwestern United States, salt deposits of the Permian basin underlie large parts of Kansas, Texas, Oklahoma and New Mexico. In Southeast New Mexico, the Salado Formation is actively being mined for potash and is also the site of the Waste Isolation Pilot Plant (WIPP), a geologic repository located 2,150 feet below surface. Although the Salado Formation consists mainly of halite, other phases exist (Madsen 1966; Lambert 1992), including calcium, potassium and magnesium-bearing chlorides and sulfates. Among these are sylvite (KCl), carnallite ($KMgCl_3 \cdot 6H_2O$), langbeinite [$K2Mg_2(SO_4)_3$], leonite [$K_2Mg(SO_4)_2 \cdot 4H_2O$], polyhalite [$K_2Ca_2Mg(SO_4)_4 \cdot 2H_2O$] and gypsum [$CaSO_4 \cdot 2H_2O$].

The waste currently isolated in WIPP is transuranic (TRU) waste, but other types of waste, including those containing fission products (FP's), may be disposed in a future repository similar to WIPP. In such a hypothetical scenario, the concentration of FP's may be high enough to cause heating of the near-field. Intrusion of groundwater into the disposal vault will initially dissolve the salt phases and may also dissolve waste packages, thereby mobilizing radionuclide elements, including FP's, such as ^{135}Cs, ^{137}Cs, ^{90}Sr, and ^{129}I. As salt phases in the formations dissolve, the solution will become saturated with new phases. Transport of material in solution away from the heat source may result in precipitation of salt phases, which may sequester FP's into their mineral structures. For example, the potassium-bearing phases, such as carnallite, langbeinite, leonite and sylvite could potentially uptake Cs because of the similarity in ionic size between K^+ and Cs^+ (196 and 168 pm, respectively; both 12-fold coordination). In addition, precipitation of gypsum ($CaSO_4 \cdot 2H_2O$), could sequester large amounts of strontium because of the similarity in ionic size between Sr^{2+} and Ca^{2+} (133 and 120 pm, respectively; both at 8-fold coordination). Finally, Cl^--bearing phases, such as sylvite and carnallite, may uptake iodine, with the substitution of I^- for Cl^- (220 and 181 pm, respectively).

Surprisingly, few data exist on the partitioning of Cs^+, Sr^{2+} and I^- into evaporite-type salt phases. For example, Matsuda (1958), Merback & Gonella (1969), and Schock & Puchelt (1971) all reported only minor uptake of Cs into sylvite, but Matsuda (1958) and Malikova (1967) demonstrated that Cs^+ and Rb^+ (an element similar in behavior to both K^+ and Cs^+) were significantly sequestered into carnallite. In the study by Malikova (1967), uptake of Rb^+ into carnallite increased with increasing temperature. However, no data exists on the partitioning of Cs^+ between langbeinite, leonite or similar K-bearing sulfate phases. Partitioning of Sr^{2+} between gypsum and solution was reported by Kushnir (1980) and Ichikuni & Musha (1978). These authors conducted experiments only at relatively low temperatures (up to 60 ºC). Last, no direct quantitative experimental data were found describing partitioning of iodine between salt phases and solution.

5.2 Experimental Process Description

5.2.1 Overall Strategy and Process

Distribution coefficients were obtained in well-controlled experimental systems by measuring the concentration of an element in solution and in the solid phase. In many previous studies the

concentrations of trace and major elements in the solid phase were determined by first separating the solid from solution and then re-dissolving the solid into a solution and then analyzing it for trace and major elements. The distribution coefficient, *D*, is defined as:

$$D = \frac{\left[{}^{(C_S^{TE})}/_{(C_S^{ME})}\right]}{\left[{}^{(C_L^{TE})}/_{(C_L^{ME})}\right]} \quad (5.1)$$

where C_S^{TE}, C_S^{ME}, C_L^{TE}, and C_L^{ME} represent the concentration of the trace element in the solid, the major (or "carrier") element in the solid, the trace element in the liquid (aqueous solution), and the major element in the liquid, respectively. The "carrier" element is the element for which the trace element is being substituted. For example, K^+ is the carrier element for Cs^+.

For systems in which a single solid phase is the only one that precipitates, this strategy works well. However, in many cases, multiple phases nucleate and precipitate from solution and it is often difficult to separate these solids, particularly when they are intergrown. In addition, there is the possibility that the trace element of interest is heterogeneously distributed in the solid. Such "zoning" is typical in many high-temperature (magmatic) systems and, in this case, only the outermost "zone" of the solid is in equilibrium with solution. In these cases, physical separation of the solid phase followed by dissolution and solution analysis would be inappropriate and a different strategy is needed.

Our strategy for obtaining accurate distribution coefficients relies on Electron Microprobe Analysis (EMPA). Crystals were separated from solution and then mounted in epoxy resin. Following curing of the resin, the encased crystals were polished using non-aqueous solutions (heptane). Our crystal specimens were processed in Sandia's low humidity dry lab by Ms. Ashley Allen (Org. 2545; Power Sources and Development, Albuquerque) in which extreme care was taken to not dissolve the crystals during the polishing phase. The advantage of EMPA is that different phases and element zoning can be distinguished using a combination of Backscattered Electrons (BSE) and Energy Dispersive Spectroscopy (EDS) that reveal the identities and distributions of elements within the crystals. Details of EMPA are discussed below.

5.2.2 Experimental Procedure

Briefly, we utilized a two-pronged strategy for precipitating the salt phases of interest from solution: 1) using natural salt phases as the starting reagents; and 2) combining research-grade chemicals in the correct stoichiometry to yield saturation of desired phases. Natural salt phases sylvite, carnallite, polyhalite, and langbeinite were graciously donated by the Mosaic Mining Company. Natural samples were carefully crushed to obtain fine powders or fragments of crystals in the millimeter size range. A portion of each salt phase was separated and set aside for characterization.

As a first method, we attempted to overgrow a "seed" crystal with new material by dissolving the fine powder into solution. After the finely-ground powder has completely dissolved, a solution containing the elements Cs, Sr, and I in low concentrations (100 to 500 ppm) were added and the large, millimeter-size "seed" crystals added to the reaction vessels. The lids of the reaction vessels were removed, allowing for evaporation of the solution until the solution became supersaturated. New growth of the phase of interest commenced and continued for several weeks until a relatively thick rind of new material precipitated onto the underlying substrate. It was hoped that the overgrowths would be readily distinguished from the "seed" crystal.

For a variety of reasons, this first strategy did not work well, so we resorted to a second approach. As stated above, the second strategy entailed mixing research-grade chemicals in stoichiometric proportions to obtain saturate the solution with the desired solid phase and cause precipitation. For example, to grow langbeinite [$K_2Mg_2(SO_4)_3$], we added K_2SO_4 and $MgSO_4$ in a 1:2 molar ratio.

Non-radioactive Cs and Sr were added to the solutions as chlorides and iodine as KI. Starting concentrations of Cs, Sr, and I were typically 100, 200 and 400 ppm. In select cases, the concentrations of the trace elements were increased to achieve a specific result. For example, the concentration of Cs in a set of sylvite precipitation experiments was increased to 10,000 ppm.

In another set of sylvite experiments the added trace element was rubidium. The purpose of this experiment was to check for consistency with previous experiments (see below). The research-grade major element and the trace element chemicals were mixed with deionized water (DIW) in 120 mL polypropylene bottles and placed in constant temperature ovens at 28, 50, 70, and 90 ºC. The bottles were uncapped for several hours each day and evaporation spurred saturation of the solutions.

In most cases, large, well-formed crystals of sylvite, langbeinite (and its lower temperature equivalents; see below), and gypsum formed and were easily separated from solution. However, in the case of carnallite [$KMgCl_3 \cdot 6H_2O$], stoichiometric solutions did not produce pure carnallite, but a physical mixture of sylvite [KCl] and carnallite, in which the former was manifested as a matrix into which the latter formed isolated inclusions. The presence of carnallite in isolated embayments between sylvite or as inclusions wholly encased by sylvite, made it unclear if carnallite was growing from a solution representative of the prepared/sampled bulk solution. Accordingly, we altered the "recipe" for growing carnallite by mixing KCl and $MgCl_2$ in a 1:6 molar ratio. Evaporation of this relatively Mg-rich solution produced large crystals of carnallite with only minor sylvite or bischoffite ($MgCl_2 \cdot nH_2O$).

Crystals were physically separated from the experiment by a spatula and then quickly rinsed with ethanol on 0.20 μm filter paper to remove any adhering solution. The crystals were then dried in weigh boats and placed into labelled containers until mounted in epoxy and polished. In the case of carnallite, the crystals were strongly hygroscopic, so they were immediately placed in a desiccator for preservation. In select samples, a portion of the crystals were set aside for characterization by Scanning Electron Microscopy (SEM) and X-ray Diffraction (XRD).

5.2.3 Electron Microprobe Analysis (EMPA)

The chemical compositions of the crystals were determined by EMPA methods. The instrument used for analysis is the JOEL JXA-8530F HyperProbe Electron Microanalyzer, which is run and maintained by Mr. Richard (Dick) Grant, Sandia, Albuquerque (Org. 01819; Materials Characterization and Performance). In brief, the instrument accelerates a focused beam of electrons onto the sample surface. The electron beam interacts with the sample by displacing electrons in the innermost shell of the nucleus of the constituent atoms, causing electrons from the outermost shells to "fill in" for the displaced electron. The change in energy of the replacement electrons is expressed as x-rays whose energies and wavelengths are characteristic of the constituent element. The concentrations of the elements were determined by comparison to well-characterized standards whose elemental concentrations are precisely known. Typical analytical conditions were 20 nanoamp current, 20 KeV acceleration potential and a spot size of 10 μm. Because the intensities of the x-rays are dependent upon the matrix used, in some cases we had to use our own standards. For these (carnallite and langbeinite), we obtained a fragment of a pure phase, dissolved it into solution and then analyzed the solution (by ICP-AES) for the constituent elements. Another fragment of the same samples was then encased in epoxy, polished and placed in a sample holder within the microprobe. Knowledge of the precise chemical composition allowed us to use these materials as standards. The advantage of EMPA over other techniques is that a small spot (~10 μm in diameter) on the sample surface can be analyzed such that small variations in chemical composition can be quantified. Because the area of exposed crystals in the sample mounts are large compared to the small beam size, we were typically able to analyze 10 to 30 individual spots on a crystal and then average the concentrations to obtain representative bulk concentrations. Concentrations of major elements (Ca, K, Mg, S, Cl, and O) were accurate to within ~2%. The lower limit of quantification (LLQ) of the trace element concentrations were typically in the range of 300 to 500 ppm; we accepted quantitative values of 3× LLQ.

The instrument is also equipped to perform Scanning Electron Microscopy (SEM) and with Backscattered Electron (BSE) and Energy Dispersive Spectrometry (EDS) detectors. These imaging/analysis capabilities allowed us to distinguish between various phases and identify the crystals of interest for quantitative analysis.

5.2.4 Solution Analyses (ICP-AES, -MS and IC)

Concentrations of major elements (Ca, K, and Mg) and Sr in the solutions were determined by Inductively-Coupled Plasma Atomic Emission Spectrometry (ICP-AES). Inductively-Coupled Plasma Mass Spectrometry (ICP-MS) was used to determine concentrations of Cs and Rb. In the case of Cs, it is possible to accurately analyze concentrations in the 100 to 200 ppb range, with the calibration curve of 10 to 200 ppb. Low concentrations are needed in the experiments, to maintain Cs at trace levels and to make allowance for sample dilution. Concentrations of anions in solution (SO_4^{2-}, Cl^-, and I^-) were determined by Ion Chromatography (IC) methods. In all cases, the concentrations of anions in solution were well above the LLQ of the instrument.

5.2.5 X-ray Diffraction (XRD)

As stated above, aliquots of the harvested solids were set aside for phase identification by XRD methods. The samples were ground into a fine powder and pressed into specially manufactured low background holders. The powders were analyzed by a Bruker D8 Advance XRD unit using Cu Kα radiation over a 2-theta interval of 10 to 80 degrees. Phase identification was confirmed using the PDF 4+ software.

5.2.6 Scanning Electron Microscopy (SEM)

Aliquots of the selected solids were imaged on a JEOL JSM-5900LV SEM. Crystals were mounted on an aluminum stub with double-side tape and coated with platinum to yield an electrically conducting surface. The SEM is also equipped with an EDS and Oxford BSE detectors, which facilitated phase identitification.

5.3 Results

5.3.1 Sylvite [KCl]

Sylvite typically precipitated as equant hopper-type crystals. Imaging of sylvite shows that the crystals have a “skeletal” appearance (Figure 9). Analyses of the crystals revealed that concentrations of Cs and Sr were below their respective LLQ’s. On the other hand, low but quantifiable concentrations of I were detected.

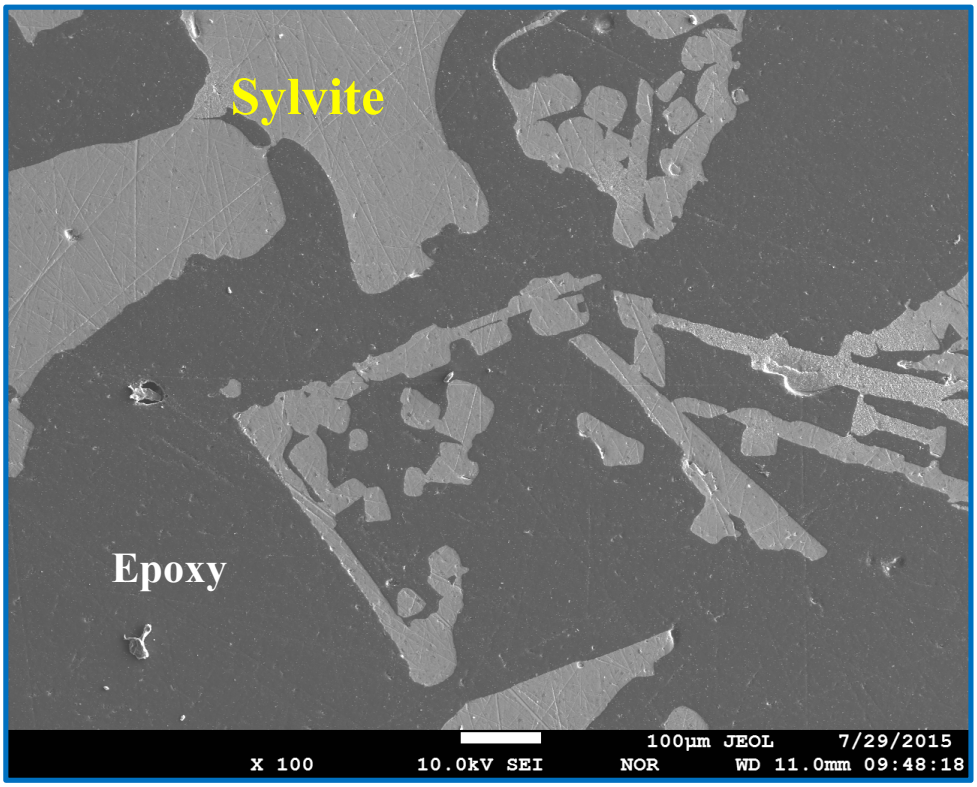

Figure 9. SEM image of typical sylvite crystals (light grey) exhibiting "skeletal" appearance. The scale bar (100 µm) is located on the center bottom of the image.

Knowledge of the concentrations of both Cl and I in both the crystals and solution allowed us to calculate the distribution coefficient of I between sylvite and solution as 0.19. To compare the results for sylvite with previous studies (Schock and Puchelt, 1971), we ran a set of experiments in which the trace element was Rb. Concentrations of Rb in the sylvite crystals were well above the LLQ but, as of this writing, the concentrations of Rb in the solution in equilibrium with sylvite have yet to be determined.

5.3.2 Gypsum [CaSO4·2H2O]

Gypsum precipitated as acicular needles whose aspect ratios (length to width ratio) varied inversely with the concentration of Sr. In other words, when the concentration of Sr was relatively low (e.g., 200 ppm initial), the aspect ratio was high. On the other hand, as the concentration of Sr increased (up to 600 ppm initial), the aspect ratio decreased significantly. In addition, imaging of representative sets of crystals revealed the presence of celestite ($SrSO_4$) in virtually all samples (Figure 10). Celestite is manifested as small clusters of crystals that radiate out from a point on the surface of gypsum. The amount of celestite present is proportional to the amount of Sr in solution.

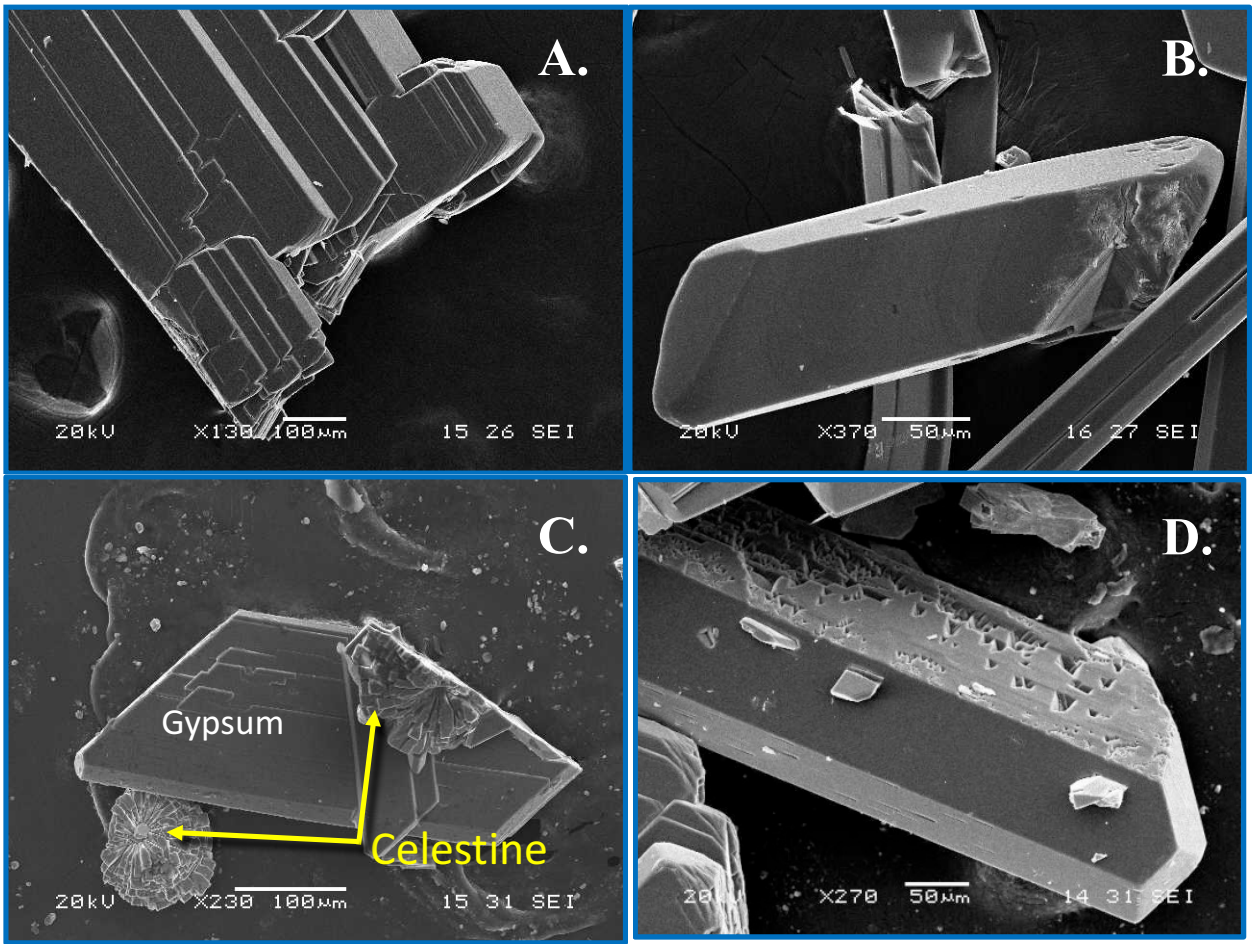

Figure 10. Typical SEM images of precipitated gypsum. With high Sr concentrations (600 ppm initial), as seen in Image C, the gypsum crystals are relatively small and are accompanied by celestite ($SrSO_4$).

In experiments with relatively low concentrations of Sr, the amount of celestite present cannot be detected by XRD analysis, and its presence is only known through imaging using SEM. BSE imaging and x-ray mapping, in which the electron beam in the microprobe rasters over the field of view and collects x-rays of a designated element, shows only slight variations in Sr concentration between crystals (Figure 11).

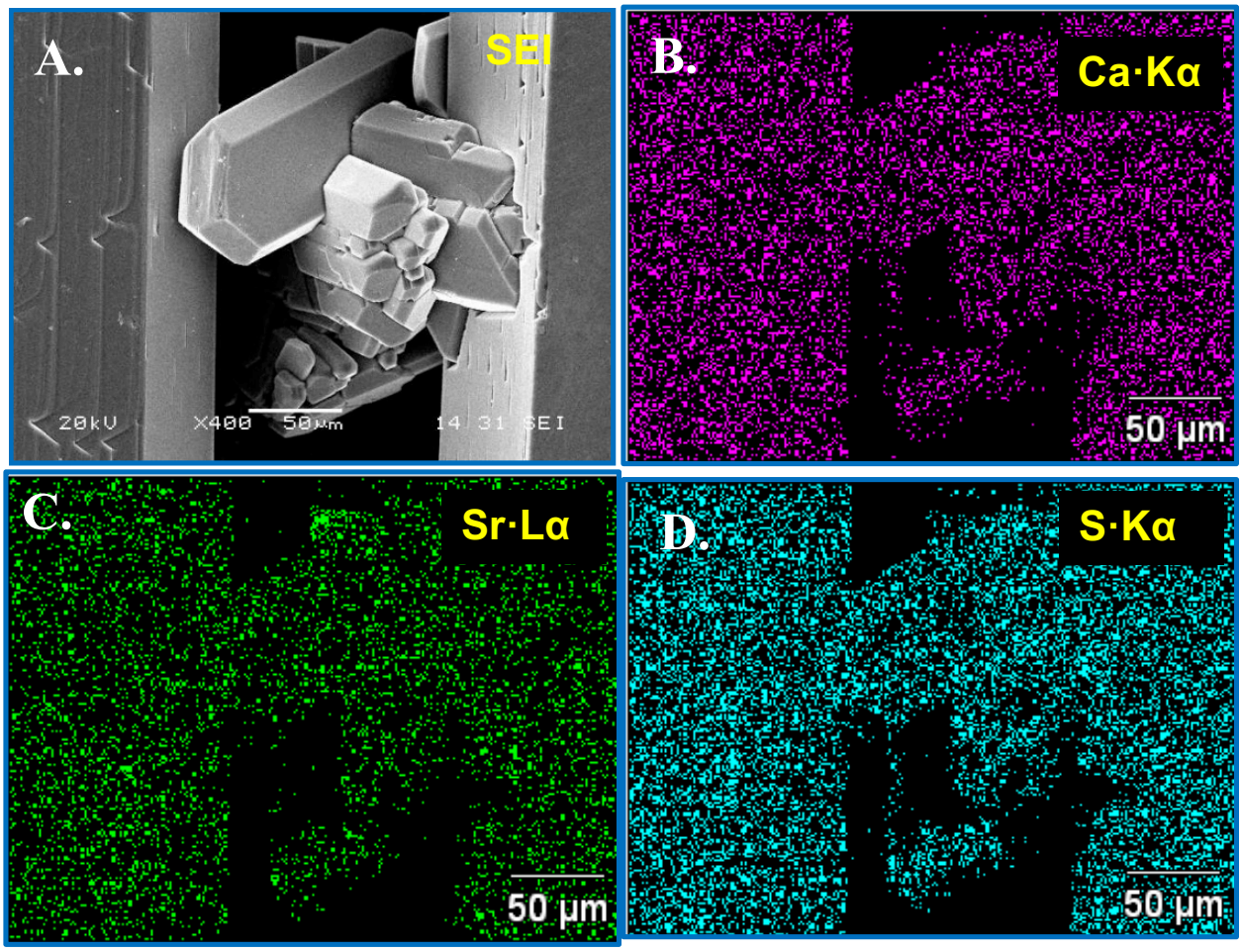

Figure 11. SEM image of gypsum (A) and corresponding x-ray maps illustrating the distribution of Ca, Sr, and S (B, C and D, respectively) in the crystals.

Multiple crystals in each sample were therefore selected for analyses to capture the variation in Sr concentration. It turns out that the variations are generally minor (10 to 20% relative). In every sample at every temperature (28 to 90ºC), the concentration of Sr is well above its LLQ In general, the concentration of Sr in gypsum did not vary greatly with temperature. As of this writing, the concentrations of Sr in solution are not yet available. In select experiments, we doped the solution with iodine, to test if this anion can substitute into the crystal lattice of gypsum. We did not expect to see much substitution of I, because the iodate anion (IO_3^-) would have to somehow substitute for sulfate (SO_4^{2-}). A proposed coupled substitution is:

$$K^+ + IO_3^- = Ca^{2+} + SO_4^{2-} \quad (5.2)$$

Because of the geometry of the iodate ion (planar, 3-fold symmetry) is very different than that of sulfate (tetrahedral symmetry), the energetics of this substitution would be unfavorable. In fact, we found no evidence for iodine substitution into gypsum (concentrations of I in gypsum were below its LLQ).

5.3.3 Langeinite [$K_2Mg_2(SO_4)_3$] (or the K_2SO_4-$MgSO_4$-H_2O System)

Langbeinite [$K_2Mg_2(SO_4)_3$] is an important economic phase in the Permian Salado formation. It is mined for potash, and is valued because of its relatively slow dissolution rate and lack of chloride. However, langbeinite is stable only at relatively high temperatures (>70ºC) (Wollmann and Voigt, 2010). Between ~70 and 50ºC leonite [$K_2Mg(SO_4)_2 \cdot 4H_2O$] is stable and below ~50ºC picromerite [$K_2Mg(SO_4)_2 \cdot 6H_2O$] is

the equilibrium phase. Thus, it is probably more useful to discuss the results in terms of the K_2SO_4-$MgSO_4$-H_2O system rather than "langbeinite". Experiments conducted at 90ºC yielded both leonite and langbeinite. This apparent contradiction can be (partially) reconciled by the observation that leonite appears to be nucleating first, but then is resorbing to form langbeinite (Figure 12). Large multiphase masses of crystals precipitated at 90ºC.

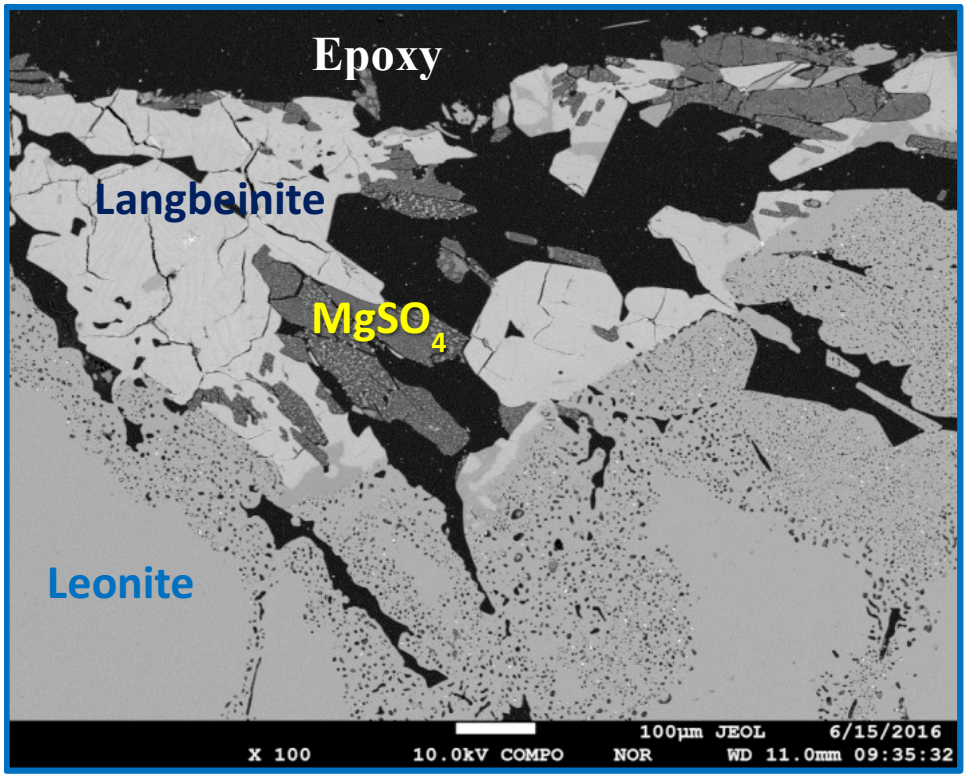

Figure 12. Backscattered electron image of precipitates from an experiment at 90 ºC. Light grey represents langbeinite, medium grey leonite, dark grey $MgSO_4$ and black epoxy. Note the porous rim around the edge of the leonite indicating it is unstable.

Material that appears to be leonite is manifested as long thin "bladed" crystals whereas langbeinite is expressed as cubic crystals with indistinct habit. Partitioning of Cs for K is moderate for langbeinite at 90ºC with partition coefficients between 0.40 to 1.70. When leonite and langbeinite coexist (even when leonite is metastable), partitioning appears to favor langbeinite (Figure 13 and Figure 14). Partition coefficients for Cs/K between leonite and solution are between 0.40 and 1.39.

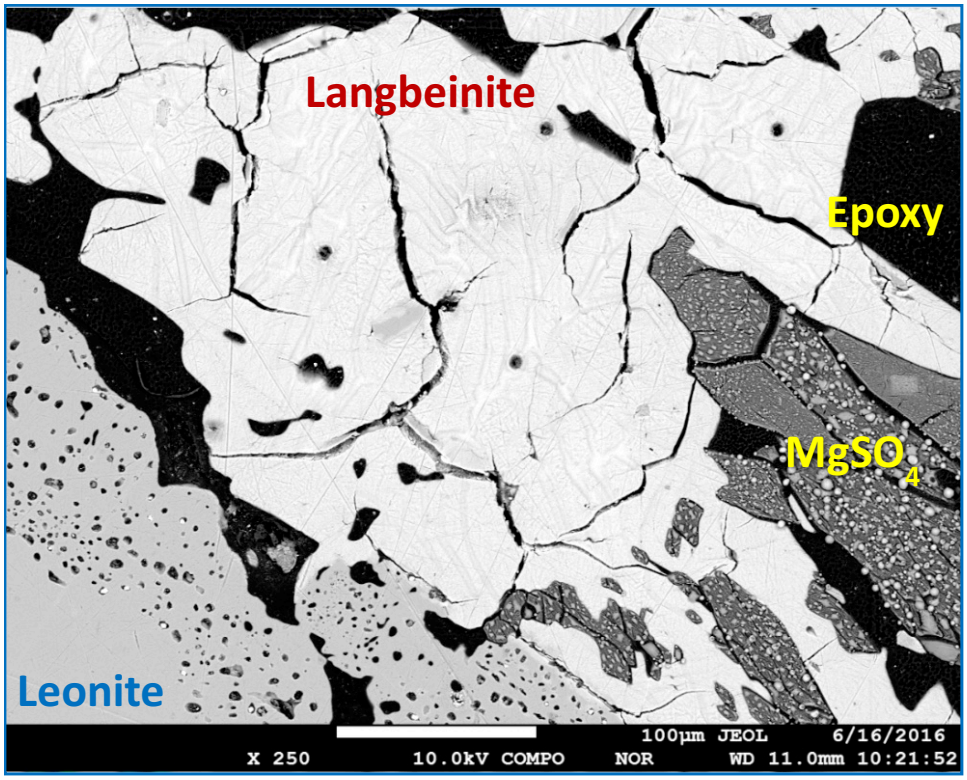

Figure 13. Backscattered electron image of a langbeinite crystal (light grey) surrounded by porous leonite (medium grey), $MgSO_4$ (dark grey) and epoxy (black).

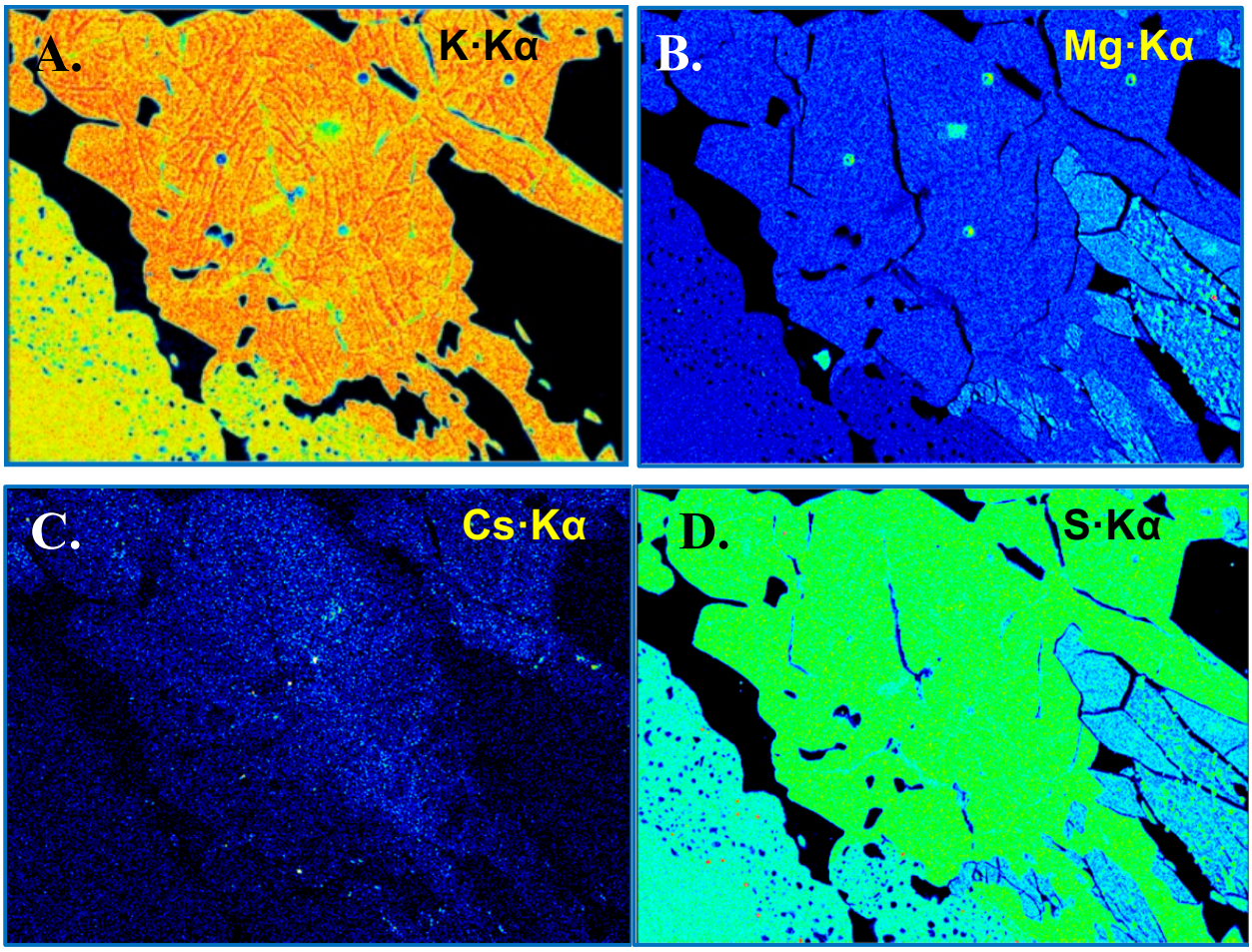

Figure 14. X-ray maps of langbeinite (same as depicted in Fig. 5). K Kα (A), Mg Kα (B), Cs Lα (C) and S Kα (D). The x-ray maps indicate that Cs is relatively homogeneously distributed in the langbeinite and that more Cs is present in langbeinite compared to leonite.

At lower temperatures, leonite predominates and partitioning of Cs is about the same (0.4 to 2.10, but is only based on two samples). Below 70ºC, picromerite is the stable phase and is manifested as large, clear prismatic crystals. Surprisingly, picromerite does not uptake Cs. Thus, the stable phases at higher temperatures, langbeinite and to a lesser degree leonite, harbor low to moderate concentrations of Cs, but at lower temperatures (<50 ºC), the phases in this system do not host Cs. Experiments in which iodine was the dopant revealed virtually no uptake of I into langbeinite, leonite, or picromerite.

5.3.4 Carnallite [$KMgCl_3 \cdot 6H_2O$]

With an excess of Mg in the starting solution (see Section 5.2.2, above), evaporation of solutions produced large crystals of carnallite with a variety of crystal habits (Figure 15). Examination of the run products by SEM and EMPA showed that most of the precipitates were carnallite with minor amounts of sylvite and bischoffite.

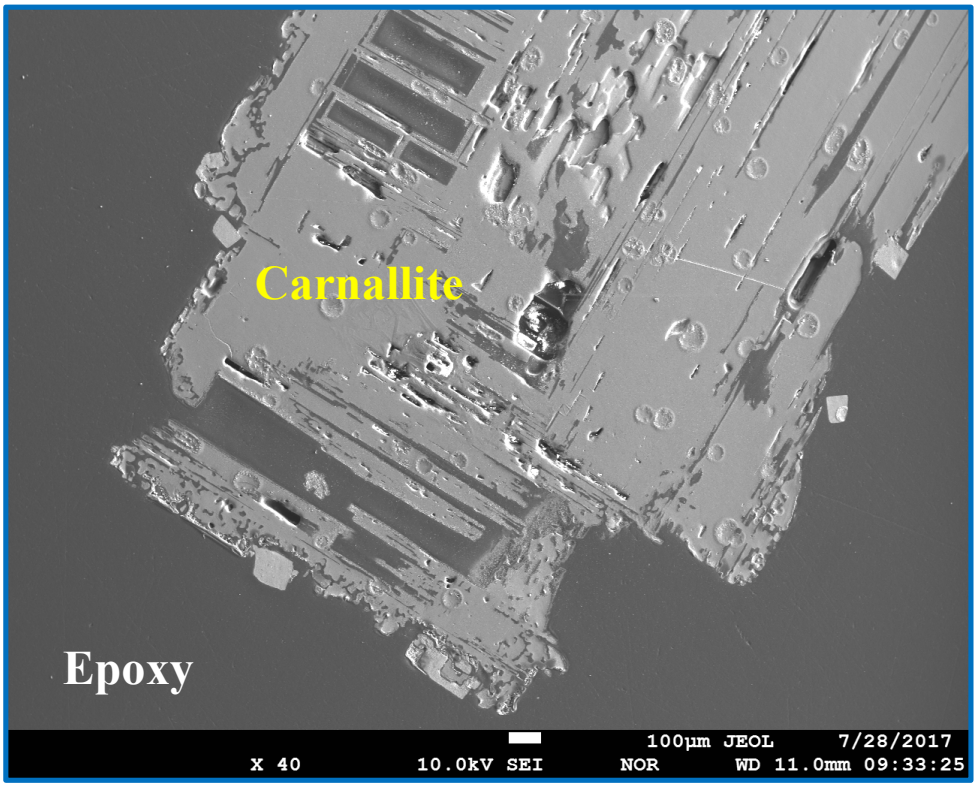

Figure 15. SEM image of a large carnallite crystal. The scale bar (100 µm) is located on the center bottom of the image.

Analyses of carnallite reveals a surprisingly strong uptake of Cs at all temperatures. The carnallite experiments were inadvertently doped to higher concentrations of Cs (200 to 800 ppm) and Cs is easily detected in carnallite by EMPA. In some cases, concentrations of Cs are as high as 10 wt.%. At these concentrations, Cs ceases to behave as a trace element, and acts instead as a major structural component. Computed distribution coefficients vary between 0.55 and 2.3. However, higher values are expected foro experiments in which carnallite samples contain high concentrations (up to 10 wt.% Cs). If this is the case, we will evaluate whether or not the distribution of Cs between crystal and solution is truly coverned as a trace component. In addition, it is not clear yet if the variation in distribution coefficients is due to differences in the Mg/K ratio, as suggested by Schock & Puchelt (1971). What is clear is that carnallite is a major host for cesium and, unlike the K_2SO_4-$MgSO_4$-H_2O system, carnallite harbors high concentrations of Cs at lower temperatures. Experiments in which iodine was the dopant reveals a low affinity for iodine in the carnallite structure. Distribution coefficients for I between carnallite and solution are ~0.17.

5.4 Conclusions and Recommendations for Future Studies

The results of this study indicate that if aqueous solutions intruded a mined salt repository and dissolved waste containing the fission products ^{135}Cs, ^{137}Cs, ^{90}Sr and ^{129}I, precipitation of typical salt phases could reduce the mobility of these FP. Specifically, precipitation of gypsum would harbor large amounts of ^{90}Sr while langbeinite and leonite would sequester moderate amounts of ^{135}Cs, ^{137}Cs at higher temperatures (>70 ºC). At all temperatures studied, carnallite is a major host for ^{135}Cs, ^{137}Cs and precipitation of this phase will greatly impact the concentration of Cs in solution. None of the phases that we studied selectively sequestered iodine.

Which phases precipitate from solution will be controlled, to a large degree, by the available concentrations of K^+, Ca^{2+}, SO_4^{2-} and, especially, Mg^{2+} (assuming saturation of halite, NaCl). The actual pathway by which the aqueous solutions evolve during evaporation, including the sequence and mass of

phases, can be computed at 25ºC, based on the work of Eugster et al. (1980). However, due to the paucity of key thermodynamic data for many candidate phases in the seven component Na-K-Mg-Ca-SO_4-Cl-H_2O system, it is not trivial to perform such calculations at temperatures above 25 ºC without simplifying assumptions. Knowledge of the stability fields of the phases in this multicomponent system as a function of temperature would facilitate a detailed model for the evolution of solution concentrations to be constructed. Note also that several other key phases, such as kainite [$KMgCl(SO_4)_3$], glauberite [$Na_2Ca(SO_4)_2$], and polyhalite [$K_2Ca_2Mg(SO_4)_4 \cdot 2H_2O$] were not included in this study. A more complete set of data could be used to consider the possibility that "natural attenuation" processes will remove much of the radionuclide load and limit the extent to which mass transport can occur. Such attenuation processes could be incorporated into safety assessments for repository systems.

5.5 References

Eugster, H.P., C.E. Harvie & J.H. Weare, 1980. Mineral equilibria in a six-component seawater system, Na-K-Mg-Ca-SO_4-Cl-H_2O, at 25ºC. *Geochimica et Cosmochimica Acta,* 44(9):1335-1347.

Ichikuni, M. & S. Musha, 1978. Partition of strontium between gypsum and solution. *Chemical Geology,* 21(3-4):359-363.

Kushnir, J., 1980. The coprecipitation of strontium, magnesium, sodium, potassium and chloride ions with gypsum. An experimental study. *Geochimica et Cosmochimica Acta,* 44(10):1471-1482.

Lambert, S.J., 1992. Geochemistry of the Waste Isolation Pilot Plant (WIPP) site, southeastern New Mexico, USA. *Applied Geochemistry,* 7(6):513-531.

Madsen, B.M., 1966. *Loweite, Vanthoffite, Bloedite and Leonite from Southeastern New Mexico*. Geological Survey Professional Paper 550, US Geological Survey, B125-B129.

Malikova, I.N., 1967. Distribution of rubidium, thallium and bromine in potassium salt deposits. *Akad. Science USSR Sibir. Sect. Inst. Geol. Geophys. Novosibirsk*, 149 pp.

Matsuda, S., 1958. On the rubidium and cesium in carnallite. *Journal of the Mineralogical Society of Japan,* 3:339.

Merbach, A. & J. Gonella, 1969. Contribution à l'étude du système quaternaire KCl—RbCl—CsCl—H_2O; I. Les isothermes de 25° des systèmes ternaires limites. *Helvetica Chimica Acta* 52:69-76.

Pierce, W.G. & E.I. Rich, 1964. *Summary of Rock Salt Deposits in the United States as Possible Storage Sites for Radioactive Waste Materials*. Geological Survey Bulletin 1148, Washington, D.C.: US Geological Survey, 91 pp.

Schock, H.H. & H. Puchelt, 1971. Rubidium and cesium distribution in salt minerals—I. Experimental investigations. *Geochimica et Cosmochimica Acta,* 35:307-317.

Wollmann, G. & W. Voigt, 2010. Solid-liquid phase equilibria in the system K_2SO_4-$MgSO_4$-H_2O at 318 K. *Fluid Phase Equilibria* 291(2):151-153.